

AperTO - Archivio Istituzionale Open Access dell'Università di Torino

## Interacting internal waves explain global patterns of interior ocean mixing

### This is the author's manuscript

*Original Citation:*

*Availability:*

This version is available <http://hdl.handle.net/2318/2028070> since 2024-10-23T15:22:08Z

*Terms of use:*

Open Access

Anyone can freely access the full text of works made available as "Open Access". Works made available under a Creative Commons license can be used according to the terms and conditions of said license. Use of all other works requires consent of the right holder (author or publisher) if not exempted from copyright protection by the applicable law.

(Article begins on next page)

# Interacting internal waves explain global patterns of interior ocean mixing

Received: 24 October 2023

Accepted: 9 August 2024

Published online: 29 August 2024

 Check for updatesGiovanni Dematteis<sup>1,2</sup>✉, Arnaud Le Boyer<sup>3</sup>, Friederike Pollmann<sup>4</sup>, Kurt L. Polzin<sup>2</sup>, Matthew H. Alford<sup>3</sup>, Caitlin B. Whalen<sup>5</sup> & Yuri V. Lvov<sup>6</sup>

Across the stable density stratification of the abyssal ocean, deep dense water is slowly propelled upward by sustained, though irregular, turbulent mixing. The resulting mean upwelling determines large-scale oceanic circulation properties like heat and carbon transport. In the ocean interior, this turbulent mixing is caused mainly by breaking internal waves: generated predominantly by winds and tides, these waves interact nonlinearly, transferring energy downscale, and finally become unstable, break and mix the water column. This paradigm, long parameterized heuristically, still lacks full theoretical explanation. Here, we close this gap using wave-wave interaction theory with input from both localized and global observations. We find near-ubiquitous agreement between first-principle predictions and observed mixing patterns in the global ocean interior. Our findings lay the foundations for a wave-driven mixing parameterization for ocean general circulation models that is entirely physics-based, which is key to reliably represent future climate states that could differ substantially from today's.

Turbulent vertical mixing in the ocean occurs when intermittent turbulent eddies smaller than a few meters, so-called oceanic microstructures, are generated in stratified regions through shear or convective instabilities. In the ocean's interior, these instabilities are primarily caused by the breaking of internal waves—energetic oscillations free to propagate through the density-stratified ocean bulk. Providing a mechanism for dense water to slowly rise from the deep ocean<sup>1,2</sup>, internal wave-driven vertical mixing is generally believed to be one of the main drivers of the oceanic circulation<sup>2,3</sup>. It thus shapes the Earth's climate<sup>4–6</sup>, influencing, among others, sea level rise<sup>7</sup>, nutrient fluxes and hence marine ecosystems<sup>8</sup>, and anthropogenic heat and carbon uptake<sup>9</sup>.

The small scales (below a few meters) and intermittent nature (timescales of minutes to hours) of turbulent mixing imply that it is both difficult to observe directly and impossible to resolve in ocean general circulation models (OGCM), whose grid cells are substantially larger than the dominant turbulence length scales. Methods that allow

us to infer wave-induced mixing from far more easily obtainable observations at larger scales (from a few to hundreds of meters)—the so-called finestructure—are hence central to advancing our understanding of ocean mixing processes and how to best parameterize them in numerical models<sup>2,10</sup>.

The state-of-the-art method to infer internal wave-driven mixing is to interpret turbulent mixing as the energy sink at the end of a downscale energy cascade through the oceanic internal wavefield, fueled by large-scale forcing and sustained by wave-wave interaction processes<sup>11–14</sup>. This picture was initially supported by formal theory<sup>11,12</sup> and ray-tracing numerical simulations<sup>15</sup> and then captured heuristically by the Finescale Parameterization (FP) formula<sup>16–19</sup>, essentially in the following form:

$$\epsilon = \epsilon_0 \frac{f N^2 \mathcal{E}^2}{f_0 N_0^2 \mathcal{E}_0^2}, \quad (1)$$

<sup>1</sup>Dipartimento di Fisica, Università degli Studi di Torino, Torino, Italy. <sup>2</sup>Physical Oceanography Department, Woods Hole Oceanographic Institution, Woods Hole, MA, USA. <sup>3</sup>Scripps Institution of Oceanography, University of California San Diego, La Jolla, CA, USA. <sup>4</sup>Institut für Meereskunde, Universität Hamburg, Hamburg, Germany. <sup>5</sup>Applied Physics Laboratory, University of Washington, Seattle, WA, USA. <sup>6</sup>Department of Mathematical Sciences, Rensselaer Polytechnic Institute, Troy, NY, USA. ✉e-mail: [giovannidematteis@gmail.com](mailto:giovannidematteis@gmail.com)

allowing for an estimation of mixing metrics—here, the turbulent kinetic energy (TKE) dissipation rate  $\epsilon$  associated with the decay time of the small-scale turbulent eddies—from characteristics of the internal wavefield: its shear-variance level  $\mathcal{E}$  (related to the energy level  $E$ ), the local Coriolis frequency  $f$ , and the buoyancy frequency  $N$ . The subscript 0 denotes reference values. Phenomenological corrections due to different spectral shapes<sup>13,19,20</sup> are omitted in Eq. (1) for simplicity. We refer to Eq. (1) as the Gregg-Heney-Polzin (GHP) parameterization<sup>13</sup>, which requires input from both shear and strain spectra. Strain-based<sup>18</sup> and shear-based<sup>16</sup> versions exist – below, we will compare our results with estimates from strain-based FP. Although the internal wave-driven mixing picture is known to break down in particular locations of the ocean, notably near the ocean’s surface and bottom boundaries and in regions with strong currents, high mesoscale activity (where interactions between geostrophically balanced motions and internal waves are large), and the presence of fronts<sup>21–27</sup>, the FP framework is corroborated by substantial observational evidence around the global ocean<sup>19,28–33</sup> and is also supported by recent numerical evaluations of the scattering integral of wave-wave interactions<sup>34,35</sup>. The FP approach has made it possible to estimate global maps of  $\epsilon$ <sup>28–30</sup> in the interior ocean and to parameterize mixing in an energetically constrained way<sup>36,37</sup> in some of the newest versions of the OGCMs.

However, significant conceptual research gaps persist in the FP framework: (i) The constant  $\epsilon_0$  in Eq. (1) is empirical<sup>13</sup>, but in order to reliably represent a wide range of conditions in a changing climate<sup>38</sup> the parameterized link between internal waves and ocean mixing needs to be based on the underlying physics<sup>10</sup>; (ii) The formula centers around the 1976 version of the Garrett–Munk spectrum<sup>39</sup> (GM76) accounting for departures from it via phenomenological correction – omitted in Eq. (1) – but new observational knowledge that GM76 is one out of many realistic spectra<sup>32,33,40,41</sup> calls for a process-based formula that applies to any spectral shape indistinctly; (iii) The interpretation of Eq. (1) relies on the notion that wave-wave interactions with large scale separation dominate the energy transfers<sup>12</sup>, but this paradigm requires a nonlinearity level arguably too strong for the assumed weakly nonlinear theory to apply<sup>42</sup> and the presence of a high-frequency source not backed-up by observations<sup>13,14</sup>.

Here, we pursue the application of formal theory<sup>11,43</sup> in a way that is more flexible to address the observed variability of the oceanic internal wavefield. We show that the bare theory of wave-wave interactions (weak wave turbulence)<sup>44–46</sup> provides a systematic explanation for the close causal link between the observed global patterns of internal wave spectral energy and of turbulent vertical mixing in the ocean interior. A few comments are due on the difference from important earlier attempts to trace the FP estimates back to first principles, in the ray-tracing regime of scale separation between small-amplitude small-scale test waves and a large-scale background shear<sup>15,47,48</sup>: (i) The ray-tracing simulations are implemented in the Wentzel-Kramers-Brillouin (WKB) approximation. This requires an arbitrary scale-separation factor that is used to tune the magnitude of the estimate, whereas the weak wave turbulence framework does not assume scale separation and allows for a quantification of spectrally local transfers; (ii) The spectrally-local transports of weak wave turbulence make the results rather independent of the high-wavenumber cutoff (Supplementary Information), vs a high sensitivity to the cutoff scale in the eikonal nonlocal transports<sup>48</sup>; (iii) Both are weakly nonlinear theories and suffer from high levels of nonlinearity as the high-wavenumber cutoff is approached, but our analysis (Supplementary Information) shows that nonlinearity is not as high as Holloway’s objection<sup>42</sup> depicted it. An updated rigorous analysis on the eikonal approach is found in refs. 49,50.

We synthesize our findings into an adaptive parameterization that generalizes the FP formula and provides an expression that is based unambiguously (without tunable parameters) on the ocean’s primitive

equations themselves instead of empirically established numbers. Crucially, we depart from the concept of a universal spectrum and fully encompass the observed variability of oceanic internal wave spectra, including an extra degree of freedom for the near-inertial spectral content, which has not yet been included in a theoretical framework before beyond a brief mention in ref. 19. Moreover, the inter-scale energy transfers that we quantify and characterize turn out to be dominated by spectrally-local interactions rather than scale-separated ones, to require large-scale energy sources consistent with observations, and to occur in a weakly nonlinear regime for most of the internal wave scales. We then corroborate our results with data from some of the most advanced oceanographic field programs, finding near-ubiquitous agreement between our theoretical predictions, input from direct microstructure observations, and other pre-existing estimates from FP methods.

## Results

### Global variability of internal wave spectra

We describe the spatially and temporally observed oceanic variance as an internal wavefield—purposely discard any vortical modes influence on such variance—and characterize this internal wavefield in the two-dimensional (2D) frequency ( $\omega$ ) and magnitude of vertical wavenumber ( $m$ ) spectral space. Internal waves oscillate with frequencies between  $f$  and  $N$ , and vertically between the first mode,  $m_0$  (inverse ocean depth), and the largest available mode that is not subject to shear instability<sup>2</sup>,  $m_c$  (see Eq. (3)).

The energy spectrum,  $e(m, \omega)$ , represents the averaged distribution of energy in the internal-wave band, so that its 2D integration over this rectangular spectral region amounts to the total internal-wave energy  $E = KE + APE$ , sum of kinetic and available potential energy. We neglect the contribution of vertical kinetic energy, thereby identifying  $KE$  with the contribution from the horizontal velocity only. To capture the variability of the internal wavefield in the ocean, we propose to represent the energy spectrum by five parameters (“Adaptive formula for the 2D spectral energy”, Eq. (4)): the high-frequency and high-wavenumber negative slopes,  $s_\omega$  and  $s_m$ ; the finite-point singularity exponent as  $\omega \rightarrow f$ ,  $s_{NI}$ , encoding the concentration of energy in the so-called inertial peak; the wavenumber scale under which the low-wavenumber energy density saturates,  $m_*$ ; and the total energy  $E = \hat{E}E_0N/N_0$ , with  $E_0 = 0.003 \text{ m}^2 \text{ s}^{-2}$ . The GM76 spectrum is recovered by setting  $s_\omega = 2$ ,  $s_m = 2$ ,  $s_{NI} = 1/2$ ,  $m_* = m^0 = 0.01 \text{ m}^{-1}$ ,  $\hat{E} = 1$ .

We estimate these five parameters (using best fit to the functional form Eq. (4), but either in frequency or in wavenumber space separately) from (a) over 2000 independent timeseries from the Global Multi-Archive Current Meter Database (GMACMD), expanding the analysis of ref. 33 to also include  $s_{NI}$  in addition to  $s_\omega$  and  $\hat{E}$  (“Global multi-archive current meter database”), and (b) 12 years worth of Argo float profiles, providing around 2.9 million estimates of wavenumber slope  $s_m$  and scale  $m_*$ <sup>32</sup> (“Argo floats”). Figure 1 illustrates the geographic location of these estimates (A) and for select observed spectra the fitting procedure to estimate  $s_\omega$  (B),  $s_{NI}$  (C),  $\hat{E}$  (D), and  $s_m$  and  $m_*$  (E).

We use this combined information to build the largest possible dataset of 2D spectral estimates of the total internal wave energy (“Combined global dataset”)—hereafter referred to as the combined global dataset. Figure 1F–J shows the histograms of the spectral parameters at those locations where all five are available after data interpolation, fitting, and analysis, representing the observed global variability of the oceanic internal wavefield.

### Wave-wave interaction theory predicts mixing

A given test wave mode can exchange energy with a pair of other modes when their amplitudes multiply each other in the quadratic term of the primitive equations of the ocean<sup>51</sup>. If nonlinearity is weak compared to linear dispersion, the energy transfers are dominated by resonant interactions, when the wavenumbers and frequencies of two

## Internal wave spectra in the global ocean

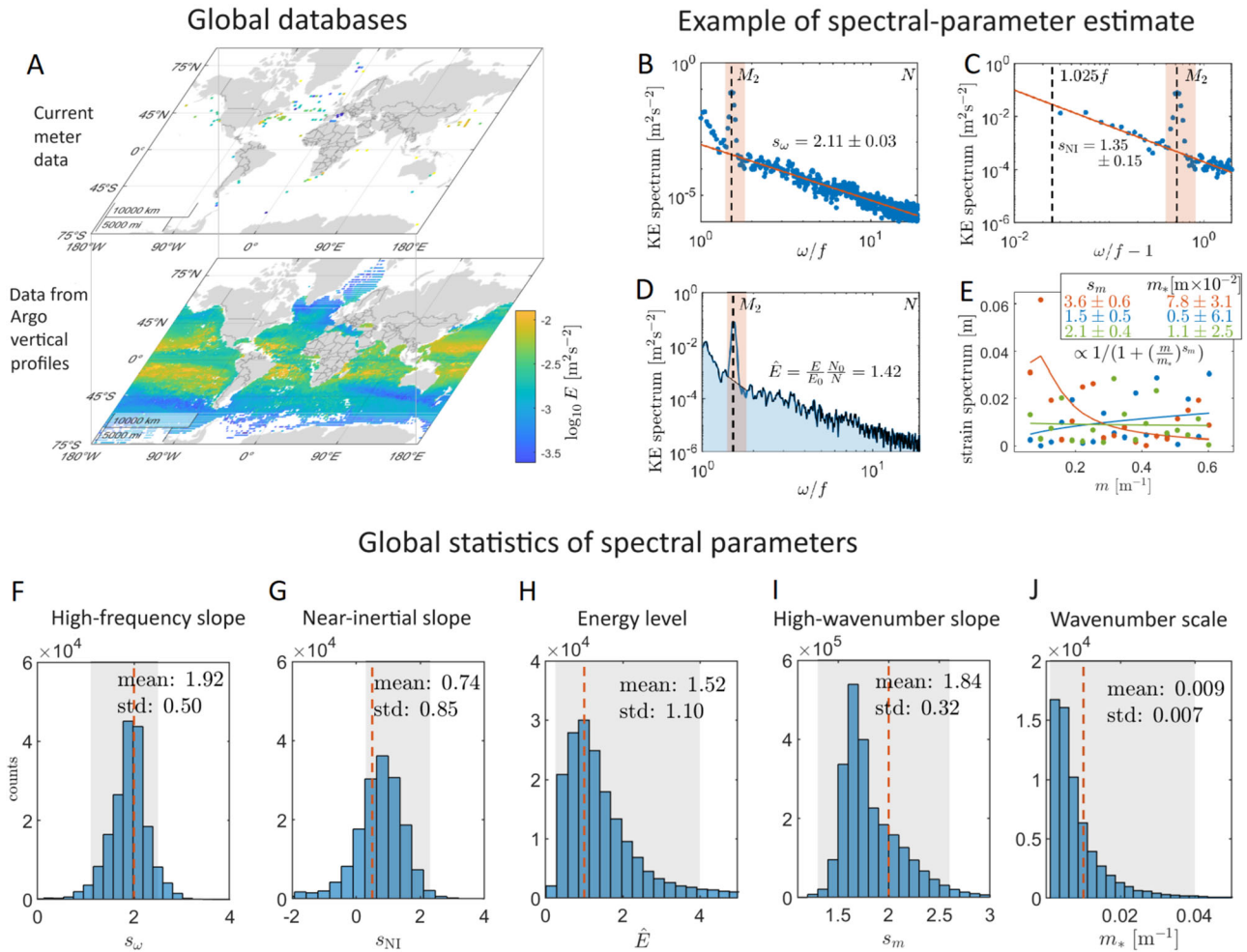


**Fig. 1 | Observed internal wave spectra and their global variability.** Input data for our global data set of two-dimensional spectral estimates of internal wave energy  $e(m, \omega)$ . **A** Illustrates data availability of total internal wave energy in the two databases used (250–500 m depth range shown), the frequency spectra from current meter observations of Global Multi-Archive Current-Meter Database (GMACMD, upper), and the vertical wavenumber spectral estimates from Conductivity-Temperature-Depth (CTD)-profiles collected by Argo floats (lower). The spectral parameters required for our theoretical model are obtained from fitting power-laws to, and integrating, the observed frequency spectra (the negative spectral “slopes” at high frequency,  $s_\omega$  in **(B)**, and low frequency,  $s_{NI}$  in **(C)**, and the

normalized total energy  $\hat{E}$  in **(D)**); notice that the  $M_2$  tidal peak is filtered out in our parameter estimation procedure, and by nonlinear curve-fitting to observed wavenumber spectra to obtain the wavenumber negative slope  $s_m$  and scale  $m_*$  **(E)**. These exemplary spectra are from measurements at 39.5°N, 54.1°W, 1006 m depth **(B–D)**; 29.6°S, 2.8°E, 589 m depth **(E, red)**; 41.6°S, 46.8°W, 589 m depth **(E, blue)**; 4.6°N, 29.1°W, 566 depth **(E, green)**. **F–J** shows the distribution of these spectral estimates for locations where all five of them are available. The grey-shaded backgrounds represent the ranges of values covered by our implementation of the theoretical formula Eq. (2), while the red dashed lines identify the canonical Garrett–Munk spectrum (GM76) parameter values.

waves sum respectively to the wavenumber and frequency of the third wave. Such interactions in internal wavefields are observed at play in the ocean<sup>52</sup>, in high-resolution models<sup>53,54</sup>, and in large water tanks<sup>55,56</sup>. We treat this triadic resonant picture rigorously in the Hamiltonian formalism derived directly from the primitive equations<sup>43</sup> (“Hamiltonian formalism of internal wave-wave interactions”). We neglect interactions of internal waves with currents and mesoscale vortices, although these can modify a purely wave-driven forward energy cascade and the resulting energy dissipation<sup>23–25,27,57</sup>, and e.g., the presence of vortices can impact the level and shape of the internal gravity wave continuum itself<sup>26,58</sup>.

To quantify the energy transfers across the different scales, we partition the internal-wave band into nine subregions (Fig. 2), using a methodology for wave-wave energy transfers between arbitrary spectral subregions<sup>59</sup> (“Wave-wave interaction transfers”). This crucially differentiates our approach from other recent work<sup>34</sup>, allowing us to target quantitatively the locality and directionality of the spectral

energy transfers. When energy is transferred to the dissipative regions, it is converted into turbulent energy<sup>2</sup>. Here, we quantify the turbulent energy production rate,  $\mathcal{P}$ , as the sum of the energy transfers leaving the internal-wave band toward the dissipative regions, as e.g., in refs. 12,34. The result is a theoretical formula for  $\mathcal{P}$ , from which we are able to evaluate the vertical diffusivity,  $K$ , and the TKE dissipation rate,  $\epsilon$ , by use of a standard parameterization Eq. (20). For  $\epsilon$ , the formula reads:

$$\epsilon = \epsilon_0^{\text{th}}(s_{NI}, s_\omega, s_m) \frac{f}{f_0} \left( \frac{Em_* s_m^{-1}}{E_0 m_*^0 s_m^{-1}} \right)^2 \quad (2)$$

An  $N^2$  factor appears when using the normalized level  $\hat{E}$ . Moreover, in the case of  $s_m = 2$ , corresponding to a white shear spectral density, we have that  $Em_*$  scales like the shear-variance level  $\mathcal{E}$ , so that Eq. (2) notably encompasses the scaling of (1) in terms of shear-variance level –while a correction arises for  $s_m \neq 2$ . In “First-principle mixing

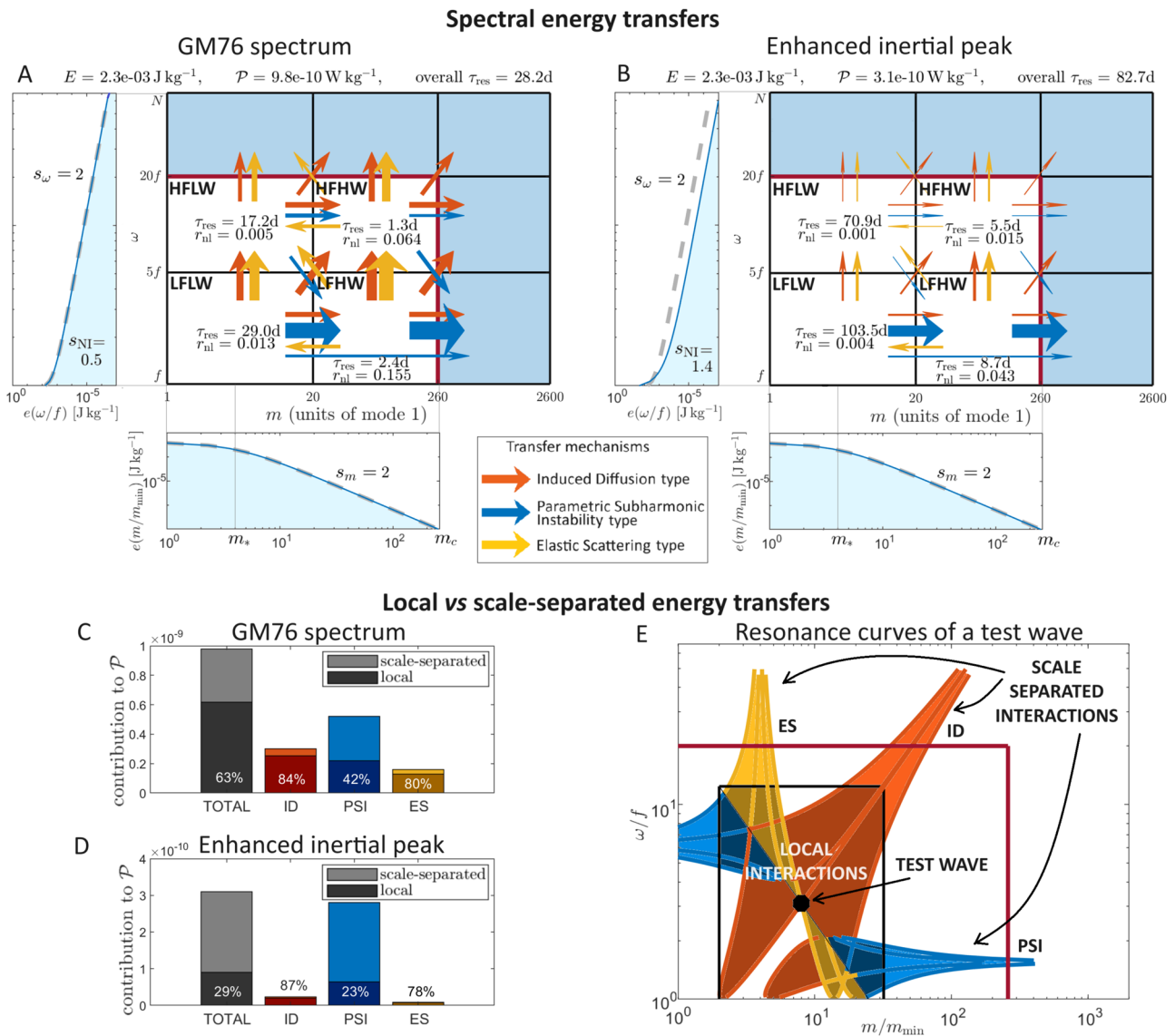


**Fig. 2 | Theoretical spectral energy transfers.** Prediction of spectral energy transfers for two exemplary spectra with same total energy  $E$  and different near-inertial slope  $s_{\text{NI}}$ . **A** Garrett–Munk model (GM76) with a shear-to-strain ratio  $R_\omega = 3$  (see Eq. (6) in “Methods”). **B** Spectrum with larger near-inertial peak ( $R_\omega = 7.3$ ). The frequency and wavenumber energy spectra are shown at the bottom and the left of (A, B), with dashed grey lines representing the GM76 reference.  $\mathcal{P}$  is the sum of the energy transfers across the red boundary separating the internal-wave band (white) from the turbulent dissipative region (light blue). For each of the subregions, we also report the nonlinear residence time  $\tau_{\text{res}}$  (ratio between the outgoing energy transfers and the energy contained in the subregion) and the nonlinearity parameter  $r_{\text{nl}}$  (ratio between the average wave period in the subregion and  $\tau_{\text{res}}$ ). We

group the interactions into the three classes of Induced Diffusion (ID), Parametric Subharmonic Instability (PSI), and Elastic Scattering (ES)—in spite of the original scale-separated definitions, here we keep track of the class also in the local regime (see (E)). The spectral subregions are labeled by the different combinations of high/low frequency (HF/LF) and high/low wavenumber (HW/LW). **C, D** show (respectively for (A) and (B)) the contributions to  $\mathcal{P}$  due to each of the mechanisms. Moreover, we quantify the proportion of such contributions that are due to spectrally local (vs scale-separated) interactions. **E** shows the energy transfers for a test wave, with the three branches and their respective local and scale-separated contributions (scale separation defined by a factor of 4 in  $m - \omega$  space).

parameterization” we provide a detailed justification of this fact, as well as the analytical relationship between our five spectral parameters and the normalized shear level of the GHP finescale parameterization<sup>13</sup>. The factor encoding the dependence on the spectral slopes is fixed by  $e_0^{\text{th}} = (1 - R_f)\mathcal{P}_0^{\text{th}}$ , with  $R_f = 0.17$ , using Eq. (20), where  $\mathcal{P}_0^{\text{th}}$  is computed numerically (“First-principle mixing parameterization”). The value associated with the original FP formula Eq. (1), of  $\mathcal{P} = 8 \times 10^{-10} \text{ W kg}^{-1}$ <sup>13</sup>, is retrieved by our theoretical prediction when we use as input the canonical parameters of the GM76 spectrum, for which we obtain  $\mathcal{P} = 9.8 \times 10^{-10} \text{ W kg}^{-1}$ . This is shown in Fig. 2A. In Fig. 2B, we then consider a different spectrum, with the same amount of energy redistributed with higher concentration in the inertial peak, and less energy in the high frequencies. We observe that this different spectral

configuration depletes  $\mathcal{P}$  considerably, by more than a factor of 3. This happens because the frequencies close to  $f$  are more linear than the high frequencies, resulting in an overall reduction of turbulent energy production. A difference in the energy pathways is also apparent in the comparison of Fig. 2A, B. We use these two cases as examples to show how different spectra imply different pathways and magnitudes of energy transfer.

We further decouple the spectral energy transfers into the three primary classes of Induced Diffusion (ID), Parametric Subharmonic Instability (PSI), and Elastic Scattering (ES)<sup>12</sup>—see “Interaction processes: classification and quantification” for more details. For the GM76-type spectrum (Fig. 2A), the PSI class is responsible for roughly half of the total turbulent energy production, but this proportion



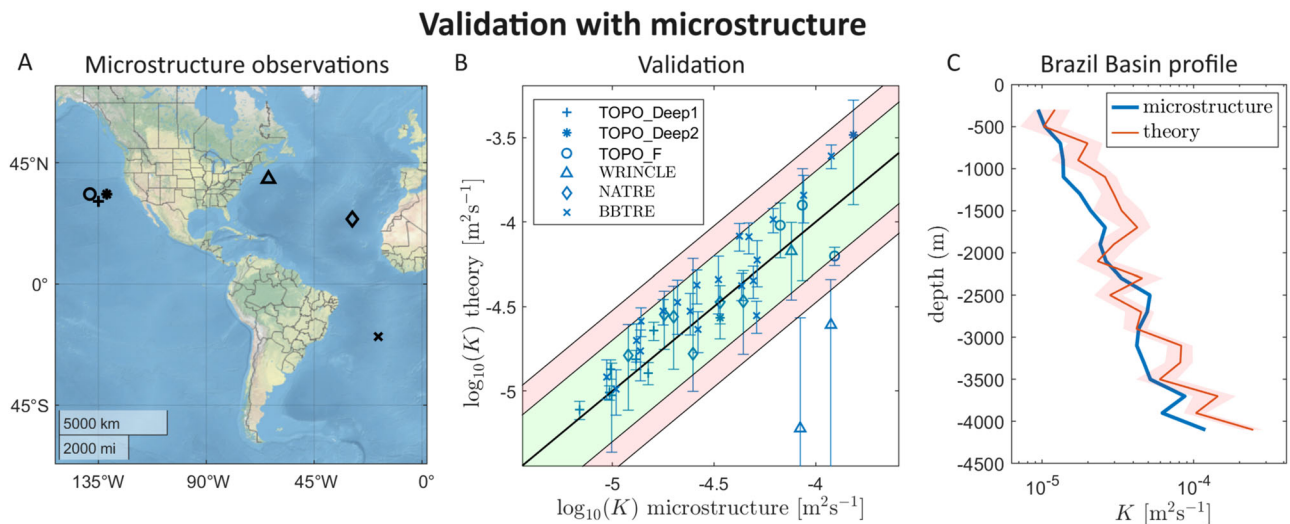


**Fig. 3 | Validation with microstructure.** **A** Location of the High-Resolution Profiler (HRP) observations used for validation. **B** Validation of the theoretical calculation of vertical diffusivity  $K$  with input from finestructure against the corresponding

microstructure estimates, from simultaneous HRP measurements<sup>19</sup>. **C** Vertical profile of  $K$  from the BBTRE observations conducted over rough topography<sup>64</sup>.

varies for different spectra (Fig. 2B). Originally, these three interaction classes were defined for the asymptotic regime of large scale separation<sup>60</sup>. Previous works, including the original FP derivation<sup>16</sup>, focus on such scale-separated interactions for estimating the energy transfers through the internal wave spectrum. Here, the resolution of the collision equation allows for an exhaustive evaluation of these three types of interaction classes to account for all interactions—we consider an interaction local if all members of the triad are within a factor of 4 from each other (either in the  $m$  or in the  $\omega$  directions), and scale-separated otherwise. For ID and ES, we find that at least 80% of the energy transfers are due to local interactions (Fig. 2C, D)—with almost negligible scale-separated contributions, in agreement with the understanding that GM76 is an asymptotic ID and an ES zero-flux solution<sup>35,61</sup>. Also for PSI, the local contribution is substantial, and Fig. 2C, D shows that the local *vs* scale-separated proportion depends strongly on the spectral distribution. This makes a difference, for instance, during the evolution of a spectrum initially forced at low frequency and low wavenumber. In such a case, we expect a transition between a regime characterized by interactions with large-scale separation at the early stages of the evolution, and a significantly more spectrally-local regime at later stages when a stationary state is reached. In general, these findings contradict the notion that the scale-separated interactions represent the total energy transfer<sup>12,16</sup> and highlight instead the role of the previously ignored interactions between waves of similar scales. This supports the results of ref. 62 to explain why there is such little observational evidence<sup>63</sup> for the suggested catastrophic decline of internal-tide energy at the latitude where PSI is most efficient<sup>53</sup>. In fact, this decline may not be as evident if the contribution by local interactions other than PSI is large and not particularly affected by the critical latitude itself.

### Validation and comparison

First, we validate the theoretical formula Eq. (2) with microstructure observations. Second, we apply Eq. (2) to the combined global dataset of internal wave spectra, compare it with strain-based FP estimates, and characterize the global distribution of mixing intensity and timescales.

**Validation with microstructure measurements.** We use time series sampled by the High-Resolution Profiler (HRP) in five distinct oceanographic regimes<sup>19</sup> (Fig. 3A and “High-resolution profiler”): in the

vicinity of a large seamount (Fieberling Guyot) in the eastern North Pacific Ocean; in a mid-ocean regime in the Atlantic; below a warm core ring of the Gulf Stream; and above the rough Mid-Atlantic Ridge in the eastern Brazil Basin. These measurements provide simultaneous independent access to micro- and fine-scales. We infer the 2D energy spectrum from the finescale shear and strain spectra (“High-resolution profiler observations”) and determine  $K$  using our theoretical formula for  $\mathcal{P}$  and the empirical relation  $K = R_f \mathcal{P} / N^2$  (“First-principle mixing parameterization”).

All except for two of 42 data points shown in Fig. 3B, each the result of an average over several profiles, agree with the microstructure estimate of  $K$ <sup>19,64</sup> within a factor of 2 (slightly more in two cases). The two outliers were measured right below a strong warm core ring, where effects not considered here such as wave-mean flow interactions are expected to enhance mixing substantially<sup>65</sup>. Considering the heterogeneity of the observations, the range of values spanning 1.5 orders of magnitude, and a nominal uncertainty of the microstructure estimates as high as 50%<sup>19</sup>, the agreement is striking.

For the BBTRE observations<sup>64</sup>, each data point comes from the average of 30 full-column profiles, in one of 20 overlying depth ranges of 200 m. This allows us to show a vertical profile of turbulent diffusivity throughout the over 4000 m-deep water column in Fig. 3C. The theoretical estimate with finestructure data input closely reproduces the microstructure vertical profile of (bottom-enhanced) mixing. Although we note an overall slight overestimate, this is comparable in size with the uncertainty on the theoretical estimate itself (shaded area in Fig. 3C).

**Mixing patterns across the global ocean interior: comparison with an existing finescale parameterization.** We apply our generalized FP (2) to the combined global dataset of internal wave spectra and compare the results to the most up-to-date strain-based FP (1) mixing estimates of ref. 30 from Argo float profiles. This reference uses the original strain-based FP incarnation of Eq. (1) with a constant  $\epsilon_0$ , which was validated against microstructure observations<sup>66</sup> and offers wider spatial coverage than the fully independent microstructure estimates used above. We sort and average our estimates in the  $1.5^\circ \times 1.5^\circ$  horizontal bins and the three depth ranges (250–500 m, 500–1000 m, and 1000–2000 m) of the Argo-based reference.

We find a total of 175 bins for which both our new (average 1023/bin) and reference (average 740/bin) estimates are available. We find

### Comparison with existing parameterization and global distributions

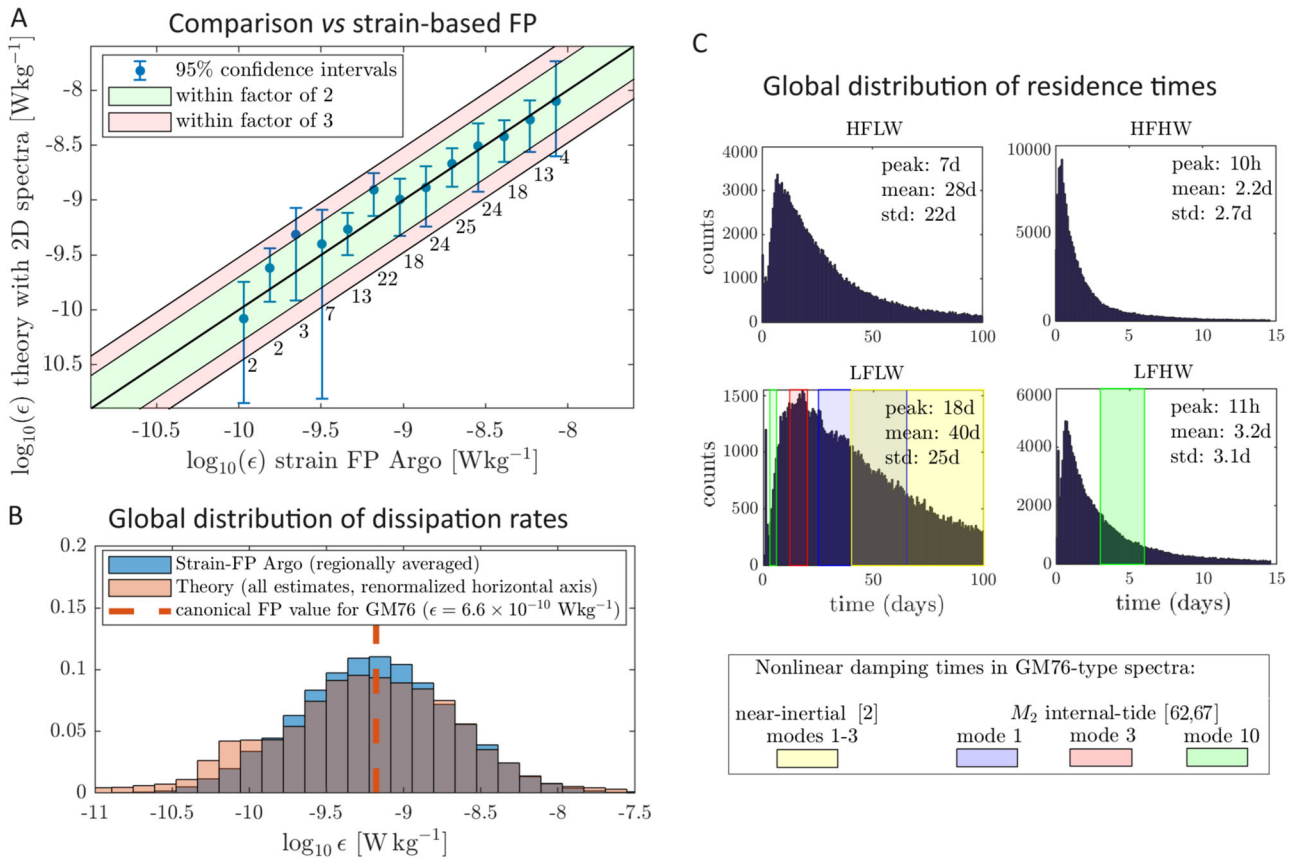


**Fig. 4 | Comparison with existing parameterization and global distributions.** **A** Evaluations of regionally and temporally averaged  $\epsilon$  in the global ocean, vs the strain finescale parameterization (FP) estimates of ref. 30. The data points where both evaluations of  $\epsilon$  are available are bin-averaged along the horizontal axis (points per bin printed below error bars). **B** Distribution of all theoretical mixing estimates for the spectra in the global combined dataset shown in Fig. 1, compared with the updated global distribution of bin-averaged values of ref. 32. To compare

on the same coarse-graining level, assuming statistical independence we renormalized the horizontal spread of the theoretical estimates, dividing by  $\log_{10} \sqrt{\bar{n}_i}$ , with  $\bar{n}_i = 1023$  estimates/bin (average). **C** Histograms of coarse-grained nonlinear residence times at the different scales of global oceanic internal wavefields. At low frequency, the shaded regions are damping-time ranges of low-modes from previous literature (mode 10, at the boundary between low and high wavenumbers, shown in both panels).

highly significant agreement over two orders of magnitude (Fig. 4A). This strengthens the success of our generalized FP (2) validated in the previous subsection. It also implies that for present-day conditions, the original FP incarnation with an empirically set constant  $\epsilon_0(l)$  provides comparable estimates to our generalized FP (2). However, for climate conditions that differ substantially from today's, only a parameterization based on the underlying physics alone like our generalized FP (2) can ensure reliable mixing estimates.

The distribution of all our calculated values of  $\epsilon$  collapses onto the distribution of the strain-based FP estimates of ref. 30 (Fig. 4B), once the spread of the theoretical estimates is suitably renormalized to account for regional coarse-graining. We now define the coarse-grained residence time,  $\tau_{\text{res}}$ , as the ratio between the total energy in a given subregion and the sum of its outgoing energy transfers. Figure 4C depicts the broad distributions of our predicted residence times, with mean values from a few days (high wavenumbers) to about 30 days (low wavenumbers). This multiscale character is reminiscent of the dual treatment of the internal tide in the OGCMs: the low-wavenumber far field, with large residence times allowing for hundreds of kilometers of propagation from the source, and the high-wavenumber near field, dissipated much faster near the generation site<sup>2</sup>. In the low-frequency panels, we show the range of wave-wave damping timescales for selected modes in GM76-type spectra: from the very weakly nonlinear low-mode near-inertial waves<sup>12</sup> (up to

100 days), to the  $M_2$  baroclinic modes spanning from 50 days (mode 1) down to a few days (mode 10)<sup>62,67</sup>. We find general consistency of our predicted timescales with prior knowledge, whilst also providing a notion of typicality of nonlinear timescales in observed oceanic conditions.

Figure 5 shows a geographical comparison between our bin-averaged theoretical estimates of TKE dissipation rate (with input from the global combined dataset) and the bin-averaged estimates from strain FP of ref. 30. Agreement is generally strong, although a few locations show some disagreement—a region-dependent study of the reasons of disagreement, which will necessarily include a combined analysis of the energy sources at play, is beyond the scope of the present manuscript and will be addressed in future work.

A study of nonlinearity level reported in Supplementary Information shows that, contrary to earlier arguments e.g., ref. 42, oceanic internal waves are typically weakly nonlinear at most scales. The scales that can involve lower residence times and higher nonlinearity levels concern the low-frequency, high-wavenumber PSI decay. Strong nonlinearity, indeed, is expected as the wave-breaking scales are approached.

### Discussion

For the sake of transparency, we underscore the constraints inherent in our approach: we (i) overlook processes other than wave-wave

## Comparison of global patterns of dissipation rate

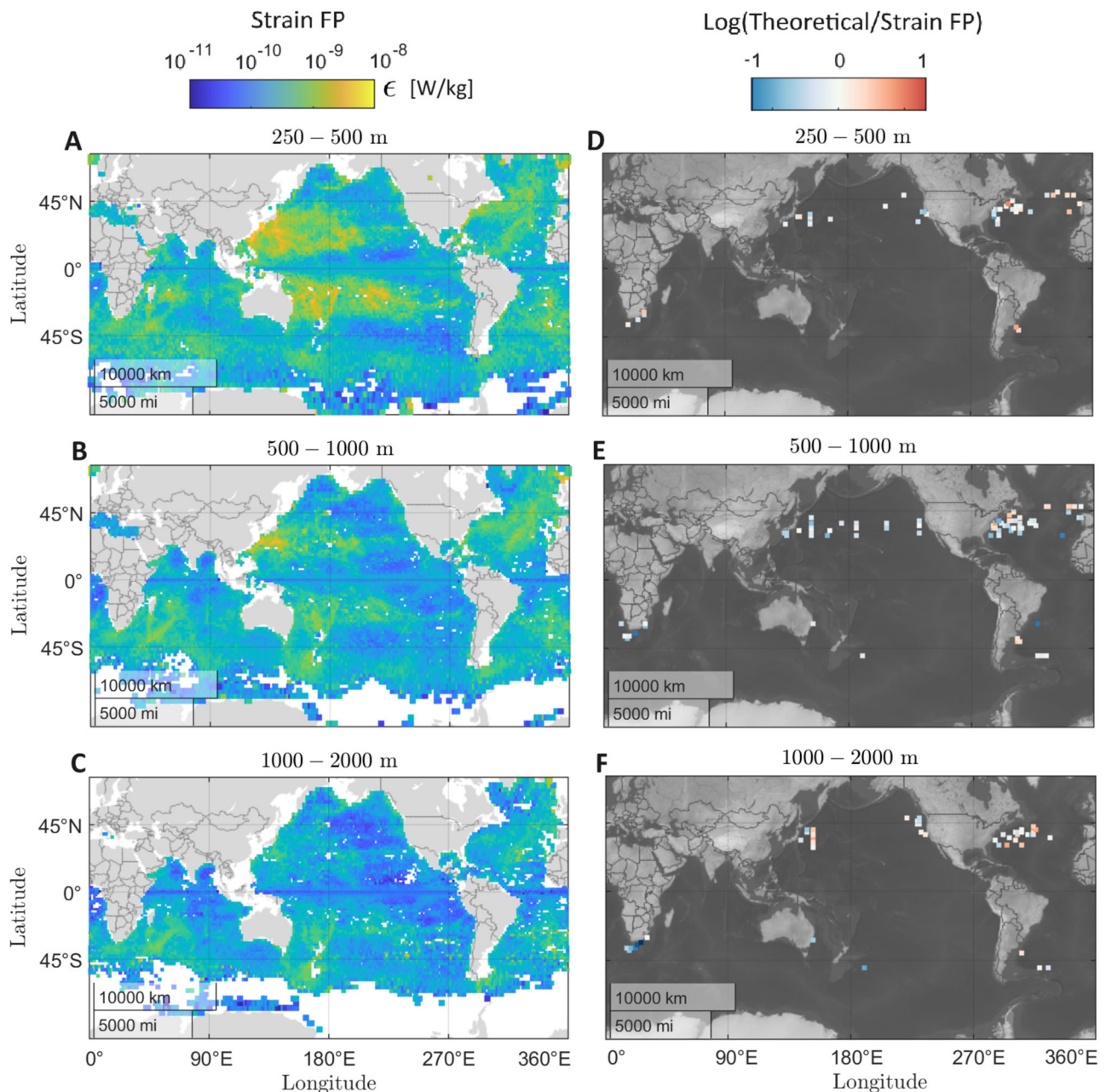


**Fig. 5 | Comparison of geographic distributions of turbulent kinetic energy dissipation rate  $\epsilon$ .** Visual comparison between the theoretical estimates of dissipation rate using our generalized finescale parameterization (FP) Eq. (2) with input from the global combined dataset, and the strain FP estimates with input from Argo data. **A–C** shows the Argo reference in three different depth levels, while **(D–F)** shows the ratio between the theoretical estimate and the Argo reference,

respectively for the three depth levels. Shown are the average values obtained over the regional bins of  $1.5^\circ \times 1.5^\circ$  horizontally, and in the three given depth layers vertically. These data points are used to build the plot in Fig. 4A. In the right panels, white color indicates agreement, while red and blue color indicate respectively a higher and lower theoretical value with respect to the strain FP value.

interactions within a spatially homogeneous, vertically symmetric, and horizontally isotropic wavefield; (ii) employ the exactly resonant formalism of weak wave turbulence theory implying, among other things, that we neglect the advective “sweeping” of small-scale waves by large-scale waves via the Doppler effect<sup>49,50</sup>; (iii) operate under the hydrostatic balance assumption; (iv) assume separable spectra—indeed an oversimplification. Moreover, (v) the weakly nonlinear assumption is arguably broken near the high-wavenumber wave-breaking threshold  $m_c$ , but the results are rather insensitive of the choice of  $m_c$ , and (vi) an assumption of regionality and stationarity

underlies our cross-matching of internal-wave spectra databases. The above points define the limitations of our approach. In particular, it cannot describe the dynamical transitions to instabilities or other non-weak phenomena that are a necessary bridge from weakly nonlinear theory to 3D turbulence, such as caustics in ray theory (related to boundary layer theory), bound waves, and transient non-resonant interactions that represent a transition to wave instability or stratified turbulence<sup>68–72</sup>. This is a topic of intense investigation from theoretical, numerical, experimental, and observational perspectives.



Our results are, at least qualitatively, in line with results from high-resolution numerical simulations, in particular regarding a high dependence on spectral shape and the large contribution from local interactions<sup>54,73,74</sup>. On the one hand, we refrain from comparing directly with previous numerical simulations restricted to a 2D vertical plane e.g., refs. 75,76, expecting the lower dimensionality to change the properties of the system by reducing linear dispersion and thereby increasing the effective nonlinearity. On the other hand, future work will need to address the comparison between different methodologies of quantification of spectral energy transfers, including triad estimates and coarse-graining methods<sup>54,59,77,78</sup>.

Within the framework of assumptions listed above, we have demonstrated that our theoretical/numerical evaluations of turbulent mixing come straightforwardly from the dynamical equations of the ocean, and are free of arbitrary parameters that could be used heuristically to fine-tune the estimates. In this sense, our quantification is from first principles in essence. Considering the apparently strong operational assumptions, it is all the more striking that our first-principle quantification of turbulent mixing (which acts as a theoretical/ conceptual generalization of the FP formula), with input from observational spectra, is in such strong agreement with widespread observations in the global ocean interior—both with direct microstructure measurements at some select locations<sup>19</sup>, and with the most up-to-date corroborated indirect estimates in the global ocean<sup>30</sup>, via strain-based FP applied to Argo data. This demonstrates the close causal link between wave-wave interactions, particularly the spectrally-local ones that were previously ignored, and turbulent mixing. This assessment paves the way for many further analyses, such as a robust study of the spatio-temporal variability of internal wave energy transfers, wave-induced mixing, and the link to environmental conditions. Such information is essential for the design of experiments or research cruises as well as the development of energy-constrained mixing parameterizations, which are indispensable for the reliable modeling of future changes in ocean dynamics and their global-scale impact<sup>4,36,38</sup>.

## Methods

### Field data

**Global multi-archive current meter database.** Ocean velocities timeseries were selected from the Global Multi-Archive Current Meter Database (GMACMD). Following ref. 33's methodology, 2260 current meters on 1362 moorings were selected (Fig. 1). The instruments' depths range from 100 m below the surface to 200 m above the seafloor with a maximum of 6431 m depth. Finally, data within 5° of the equator were discarded to avoid complications with the longer inertial periods at very low latitudes.

The time evolution of kinetic energy frequency spectra ( $\phi_{KE}(\omega)$ ) for each of these time series is evaluated using a multitaper method with a sliding 30-day window. After removing the spectral peaks associated with the main energy sources (removing frequency bands around the near-inertial and tidal peaks as well as their harmonics), the slope ( $s_\omega$ ) of the internal wave continuum is estimated with a linear fit. A similar method is used to estimate the slope ( $s_{NI}$ ) of the near-inertial peak using  $\phi_{KE}(\frac{\omega-f}{T})$ .

**Argo floats.** Argo floats autonomously profile the ocean's upper 2000 m, collecting temperature, salinity, and pressure information at a vertical resolution of a few meters roughly every 10 days e.g., ref. 79. Building on previous implementations of the finestructure parameterization<sup>28,32,80,81</sup> derived vertical wavenumber spectra of strain  $\xi_z = (N^2 - N_{fit}^2)/N^2$ , where  $N^2$  is the buoyancy frequency,  $N_{fit}^2$  a quadratic fit and  $\overline{\quad}$  the vertical mean, from these profiles, translated them into energy spectra by exploiting the polarization relations<sup>51</sup>, and fitted the GM76 model to obtain a global database of internal wave energy

level, vertical wavenumber slope  $s_m$  and wavenumber scale  $m_*$ , which we here use and are available at <https://doi.org/10.5281/zenodo.6966416><sup>82</sup>. The integrated strain spectrum provides the strain variance, a key component of the FP expression to estimate TKE dissipation rates. We here use an update of the TKE dissipation rate estimates from Argo float profiles of ref. 81, available at <https://doi.org/10.17882/9532730>.

**High-resolution profiler.** The free-falling, internally recording HRP<sup>83</sup> samples the water column giving access to spectra in vertical wavenumber space. It features an acoustic velocimeter and a Conductivity-Temperature-Depth (CTD) probe, from which we obtain the finestructure spectra of shear and strain variance, respectively. Independently, the HRP also has airfoil probes to sense the centimeter-scale velocity field. This makes it possible to reconstruct the microstructure shear variance, yielding a direct estimate of the TKE dissipation rate  $\epsilon$  and, by use of the relations Eq. (20), of the diffusivity  $K$ .

The five observational campaigns that we use are TOPO\_Deep, in the eastern North Pacific Ocean, consisting of eight profiles as deep as 3000 m; TOPO\_F, consisting of 15 profiles near TOPO\_Deep but with enhanced non-GM characteristics; the 40 WRINCLE profiles from the center of a warm core ring of the Gulf Stream; 10 profiles from the NATRE experiment, in the North Atlantic mid-ocean regime; 30 profiles from the BBTRE experiment<sup>64</sup>, conducted above the rough topography of the Mid-Atlantic Ridge in the eastern Brazil Basin. All profiles used in this analysis start at least 200 m above the bottom. Each of the 42 independent data points represented in Fig. 3B roughly corresponds to a 1-day average of multiple vertical profiles that extend in depth from 1000 m in the WRINCLE experiment to over 4000 m in the BBTRE experiment. When they belong to the same experiment, the data points come from well-separated conditions in space or time, ensuring complete statistical independence. Detailed information on the five observational campaigns is found in refs. 19,64.

### Data processing: from observations to 2D spectra

**Adaptive formula for the 2D spectral energy.** Due to the large aspect ratio of the horizontal-to-vertical scales of oceanic internal waves, a minimal statistical description of the wavefield—assuming no preferential directionality in the horizontal plane—must be two-dimensional (2D). We represent the spectra in frequency ( $\omega$ ) and magnitude of vertical wavenumber ( $m$ )—the natural dual variables for fixed-point time series and vertical stratification profiles, respectively. The internal-wave band is bounded in frequency space by the local Coriolis frequency ( $f$ ) and the buoyancy frequency ( $N$ ), and in the vertical wavenumber space by the mode-1 wavenumber  $m_0 = \pi/H$  where  $H$  is the full water column, and the wavenumber of the largest available mode that is not subject to shear instability<sup>2</sup>:

$$m_c = 2\pi/\ell_c \quad (3)$$

where  $\ell_c = \sqrt{2\text{Ri}_c KE}/N = O(10\text{m})$  is related to the critical Richardson number of Kelvin–Helmholtz instability  $\text{Ri}_c = 1/4$ , and  $KE$  is the kinetic energy density per unit of mass.

We model the total energy spectral density with the following five-parameter formula (separable in frequency and wavenumber),

$$e(m, \omega) = B \frac{\omega^{2s_{NI} - s_\omega}}{(\omega^2 - f^2)^{s_{NI}}} \frac{1}{m^{s_m} + m_*^{s_m}}, \quad (4)$$

where  $B$  is a normalization constant constrained by the total energy  $E$ . In order for  $E$  to always be finite, we assume a regularization plateau for frequency smaller than  $1.025f$ , such that  $e(m, \omega < 1.025f) = e(m, 1.025f)$ . Our justification of the plateau width is twofold: first, it is of the order of the frequency space resolution implied by our observational

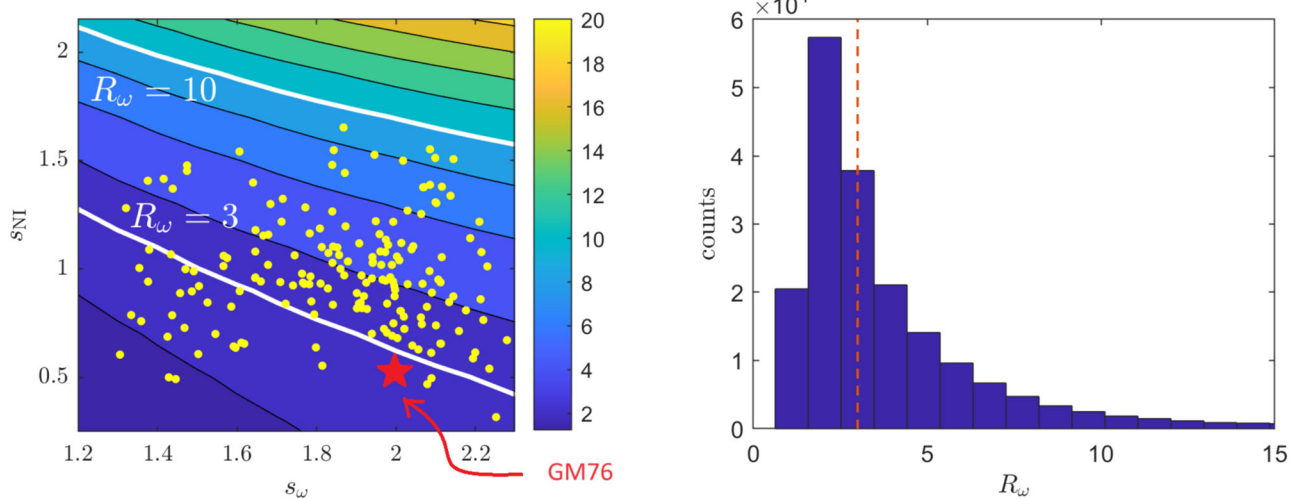


**Fig. 6 | Shear-to-strain ratio.** Left: Color map representing the shear-to-strain ratio  $R_\omega$  as a function of the spectral parameters  $s_\omega$  (high-frequency slope) and  $s_{NI}$  (near-inertial slope), according to formula (5). The yellow dots represent the spread of

bin-averaged slopes from the 175 regions in the global combined dataset. Right: Global distribution of  $R_\omega$ . The red dashed line indicates the Garrett–Munk spectrum (GM76) value of  $R_\omega = 3$ .

sliding window of 30 days (“Global multi-archive current meter database”), at mid-latitudes; second, we observe that most energy close to  $f$  (in the plateau region) is “frozen” in an effectively noninteracting linear state that does not affect the nonlinear energy transfers quantified in this manuscript (cf. Supplementary Information Fig. S2, showing residence times larger than 100 days in the inertial limit). The choices  $s_{NI} = 1/2$ ,  $s_\omega = 2$ ,  $s_m = 2$ ,  $E = 2.3 \times 10^{-3} \text{ J kg}^{-1}$  (instead of  $E = 3 \times 10^{-3} \text{ J kg}^{-1}$  because of the regularization plateau at  $f$ ),  $m = 4\pi/b$  (with  $b = 1300 \text{ m}$ ) evaluated at  $N_0 = 3 \text{ cph}$ ,  $f_0 = 2 \sin(\text{lat}) \text{ cpd}$ , at latitude  $\text{lat} = 32.5^\circ$ , reduce formula Eq. (4) to the reference GM76 spectrum. The following sections provide details on the estimate of the five spectral parameters in Eq. (4) from observational data.

**Combined global dataset.** In our global analysis of 2D internal-wave spectra, the three parameters  $s_{NI}$ ,  $s_\omega$ , and  $E$  are estimated for each moored frequency spectrum of kinetic energy computed as described in section “Global multi-archive current meter database”. By the polarization relations of internal waves<sup>41</sup>, the near-inertial spectrum of total energy (and therefore  $s_{NI}$ ) is dominated by kinetic energy, since the near-inertial waves are mostly horizontal-velocity oscillations. On the other hand, the high-frequency slope  $s_\omega$  is asymptotically the same for the kinetic and potential energy. The total energy  $E$  relates to the kinetic energy  $KE$  (neglecting vertical kinetic energy) via

$$E = KE \frac{R_\omega + 1}{R_\omega}, \quad (5)$$

where the shear-to-strain ratio  $R_\omega$  (which equals the ratio of horizontal kinetic energy to available potential energy), assuming separability, is computed as

$$R_\omega(s_{NI}, s_\omega) = \frac{1}{N^2} \frac{\int_f^N \frac{N^2 - \omega^2}{N^2 - f^2} \frac{\omega^2 + f^2}{\omega^2} \frac{\omega^{2s_{NI} - s_\omega}}{(\omega^2 - f^2)^{s_{NI}}} d\omega}{\int_f^N \frac{\omega^2 - f^2}{(N^2 - f^2)\omega^2} \frac{\omega^{2s_{NI} - s_\omega}}{(\omega^2 - f^2)^{s_{NI}}} d\omega}, \quad (6)$$

as represented in Fig. 6 (left) (see e.g., ref. 32). The yellow data points show the spread of the bin-averaged spectral slopes, with values of  $R_\omega$  always smaller than 10. This fact is important as it justifies a-posteriori the applicability of the strain-based FP in these regions, in light of the correction proposed by Ijichi and Hibiya<sup>20,48</sup>, which would be relevant only for larger values of  $R_\omega$ . The global distribution that we obtain for  $R_\omega$  is shown in Fig. 6 (right).

We complete the set of spectral parameters by assigning the average vertical wavenumber slope  $s_m$  and scale  $m$ , computed from the Argo dataset (cf. section “Argo floats”) for the discretization bin that contains the given moored spectrum. Two assumptions of statistical regionality and stationarity underlie our analysis. The results of ref. 41 indicate that the regional characterization of spectral power laws after averaging over the mesoscale-eddy space-time scales is fairly independent of the seasonal variability of  $E$ . Closer spatial correlation and seasonal variability will be analyzed in a follow-up study.

**High-resolution profiler observations.** From the HRP profiles, we obtain the finestructure spectra of shear and strain variance. We obtain directly the vertical wavenumber slope  $s_m$  and scale  $m$ , and the total energy  $E$  by use of the polarization relations and by direct calculation of  $R_\omega$  as the shear-to-strain ratio. Now, we need to infer information on the frequency slopes  $s_{NI}$  and  $s_\omega$ . To this end, we exploit the fact that  $R_\omega$  depends solely on the frequency spectrum Eq. (6) since the wave-number spectral properties cancel out in the ratio. Therefore, we have that  $R_\omega = R_\omega(s_{NI}, s_\omega)$ , as shown in Fig. 6. A given value of  $R_\omega$  therefore corresponds to a level set establishing a unique curve in the  $s_{NI}$ – $s_\omega$  plane. For an evaluation of turbulent energy production rate ( $\mathcal{P}$ ), we study the variation of the factor  $\mathcal{P}_0^{\text{th}}(s_{NI}, s_\omega, s_m)|_{s_m}$  in formula Eq. (15), at fixed  $s_m$ , along the given  $R_\omega$  level set in the  $s_{NI}$ – $s_\omega$  plane. The resulting variation turns out to be small as the level sets of  $\mathcal{P}_0^{\text{th}}(s_{NI}, s_\omega, s_m)|_{s_m}$  are mostly parallel to those of  $R_\omega(s_{NI}, s_\omega)$ , as can be appreciated in Fig. 7. The uncertainty associated with this variation is smaller than 10% in most regions of the  $s_{NI}$ – $s_\omega$  space. For operational purposes, we are thus free to fix a value of  $s_\omega$  (for simplicity, a choice of  $s_\omega = 2$  is made here), and determine the value of  $s_{NI}$  constrained by the computed value of  $R_\omega$ . The ensuing mixing evaluation is independent of the choice up to a small uncertainty.

**Theoretical methods**

**Hamiltonian formalism of internal wave-wave interactions.** We start from the simple Boussinesq approximation of the primitive equations of the ocean<sup>51,84</sup> and use the Hamiltonian formalism of ref. 43. Assuming hydrostatic balance, the dispersion relation of internal waves is given by

$$\omega^2 = f^2 + \frac{g^2}{\rho^2 N^2} \frac{k^2}{m^2}, \quad (7)$$

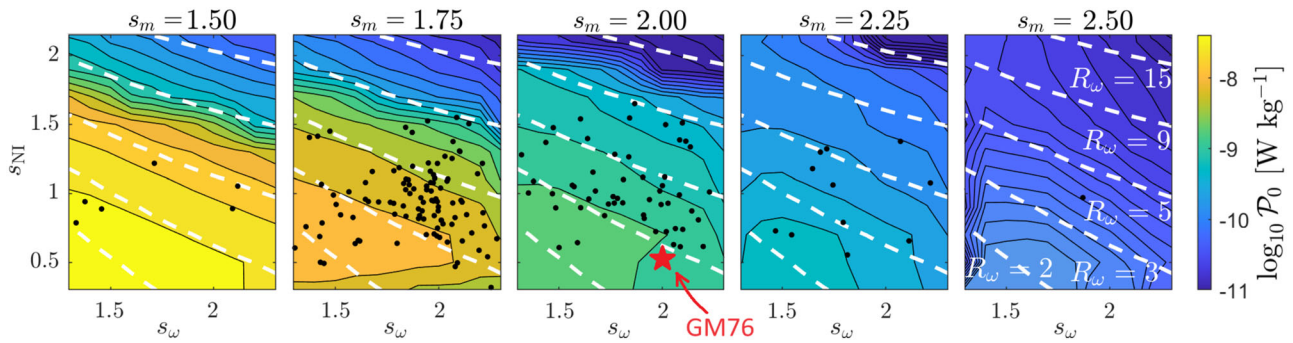


**Fig. 7 | Numerical evaluation of theoretical parameterization.** Color map of the theoretical reference turbulent production rate  $\mathcal{P}_0^{\text{th}}(s_{\text{NI}}, s_{\omega}, s_m)$ , function of the three spectral slopes (near inertial  $s_{\text{NI}}$ , high-frequency  $s_{\omega}$ , and high wavenumber  $s_m$ ), computed numerically on a grid of  $5 \times 5 \times 5$  points (cf. “First-principle mixing parameterization”). The dashed white lines are level sets of shear-to-strain  $R_{\omega}$ . When only

the shear-to-strain ratio is available,  $s_{\omega}$  and  $s_{\text{NI}}$  are not known. In that case, we exploit the fact that the level sets of  $\mathcal{P}_0^{\text{th}}$  and  $R_{\omega}$  are nearly parallel. We assign to our estimate the value of  $\mathcal{P}_0^{\text{th}}$  intercepted on the fixed level set of  $R_{\omega}$  at  $s_{\omega} = 2$  and evaluate the uncertainty error from the observed variability of  $\mathcal{P}_0^{\text{th}}$  along the level set of  $R_{\omega}$ . We find that this uncertainty is always smaller than 10% for the observed values of  $R_{\omega}$ .

where  $k$  and  $m$  are the magnitudes of the horizontal and vertical components of wavenumber,  $\rho$  is the mass density per unit of volume, and  $g$  is the acceleration of gravity. We now use isopycnal coordinates  $(x, y, \rho)$  and assume spatial homogeneity and constant potential vorticity on each isopycnal layer. For simplicity of notation, here and in the rest of section “Theoretical methods”,  $m$  denotes the vertical wavenumber in isopycnal coordinates. This reduces the equations to two field variables, the velocity potential  $\phi(x, y, \rho)$  (such that the horizontal velocity is given by  $\mathbf{u} = \nabla \phi + \nabla^{\perp} \psi$ , where  $\nabla^{\perp} = (-\partial/\partial y, \partial/\partial x)$ ), and the differential layer thickness  $\Pi(x, y, \rho) = \rho \partial z / \partial \rho$ . The divergence-free field  $\psi$  is dynamically constrained to  $\Pi$  by the constant potential vorticity assumption. The two  $\phi(x, y, \rho)$  and  $\Pi(x, y, \rho)$  are Hamiltonian canonically conjugated variables with respect to the Hamiltonian

$$\mathcal{H} = \frac{1}{2} \int dx dy d\rho \left( \Pi |\nabla \phi + \nabla^{\perp} \psi|^2 - g \left( \int_0^{\rho} \int_0^{\rho_1} d\rho d\rho_1 \frac{\Pi(\rho_2) - \bar{\Pi}(\rho_2)}{\rho_2} \right)^2 \right), \quad (8)$$

where  $\bar{\Pi}(\rho) = \rho \partial \bar{z}(\rho) / \partial \rho = -g/N^2$  is the given stratification in hydrostatic balance (here assumed constant by the vertical homogeneity assumption). This means that the equations of motion take the simple form:

$$\frac{\partial \Pi}{\partial t} = \frac{\delta \mathcal{H}}{\delta \phi}, \quad \frac{\partial \phi}{\partial t} = -\frac{\delta \mathcal{H}}{\delta \Pi}. \quad (9)$$

The Hamiltonian  $\mathcal{H}$  has a cubic nonlinearity in addition to harmonic terms. The harmonic part is diagonalized by the canonical normal variables  $a(\mathbf{p}) = N/k \sqrt{\omega(\mathbf{p})} / (2g) \Pi(\mathbf{p}) - ik/N \sqrt{g/(2\omega(\mathbf{p}))} \phi(\mathbf{p})$ , where we have now switched to Fourier space and  $\mathbf{p}$  denotes the 3D wavevector.

We now use the relationship  $\langle a(\mathbf{p}) a^*(\mathbf{p}') \rangle = n(\mathbf{p}) \delta(\mathbf{p} - \mathbf{p}')$  (the symbol  $*$  denotes complex conjugation and  $\langle \cdot \rangle$  denotes statistical average over a suitable statistical ensemble) defining the 3D wave-action spectrum  $n(\mathbf{p})$  in spatially homogeneous conditions. The 3D energy density is given by  $e(\mathbf{p}) = \omega(\mathbf{p}) n(\mathbf{p})$ , with respect to which the 2D energy density is given by  $e(m, \omega) = 4\pi(g/(\rho_0 N))^2 m^2 \omega e(\mathbf{p})$ , with  $\rho_0 = 10^3 \text{ kg/m}^3$ .

Following the standard approach of wave turbulence<sup>44,45,85</sup>, under the assumption of weak nonlinearity, in a random near-Gaussian wavefield with spatially homogeneous, horizontally isotropic, and vertically symmetric statistics, we derive the Wave Kinetic Equation for the spectral energy density<sup>11,43</sup>:

$$\dot{e}(m, \omega) = I[e, e](m, \omega), \quad (10)$$

where  $I[e, e]$  is the wave-wave collisional operator, a quadratic integral operator that accounts for the contributions from all of the possible resonant triads that involve the test wave identified by the point  $(m, \omega)$ . For details on the derivation and on the r.h.s. of Eq. (10) summarized above, we refer the reader to ref. 86. The r.h.s. of Eq. (10) has the following form<sup>43</sup>:

$$I[e, e](m_0, \omega_0) = J(m_0, \omega_0) \int [R_{12}^0 - R_{02}^1 - R_{10}^2] d\mathbf{p}_{12}, \quad (11)$$

with  $J(m, \omega) = 4\pi \rho_0^2 N^2 m^2 \omega^2 / g^2$ . The term  $R_{12}^0$  reads

$$R_{12}^0 = 4\pi n_0 n_1 n_2 \left( \frac{1}{n_0} - \frac{1}{n_1} - \frac{1}{n_2} \right) |V_{12}^0|^2 \delta(\omega_0 - \omega_1 - \omega_2) \delta(\mathbf{p}_0 - \mathbf{p}_1 - \mathbf{p}_2), \quad (12)$$

with 3D action spectrum  $n_{\mathbf{p}} = e(m, \omega) / J(m, \omega)$  and matrix elements

$$|V_{12}^0|^2 = \frac{N^2}{32g} \left\{ \left[ \frac{\mathbf{k}_0 \cdot \mathbf{k}_1}{k_0 k_1} k_2 \frac{\omega_0 \omega_1 + f_0^2}{\sqrt{\omega_0 \omega_1 \omega_2}} + \frac{\mathbf{k}_0 \cdot \mathbf{k}_2}{k_0 k_2} k_1 \frac{\omega_0 \omega_2 + f_0^2}{\sqrt{\omega_0 \omega_1 \omega_2}} + \frac{\mathbf{k}_1 \cdot \mathbf{k}_2}{k_1 k_2} k_0 \frac{\omega_1 \omega_2 - f_0^2}{\sqrt{\omega_0 \omega_1 \omega_2}} \right]^2 + \left( \frac{f_0 \mathbf{k}_1 \cdot \mathbf{k}_2}{k_0 k_1 k_2 \sqrt{\omega_0 \omega_1 \omega_2}} \right)^2 \left[ \omega_0 (k_1^2 - k_2^2) + \omega_1 (k_0^2 - k_2^2) + \omega_2 (k_1^2 - k_0^2) \right]^2 \right\}. \quad (13)$$

$\mathbf{k} = (k_x, k_y)$  denotes the 2D horizontal wavenumber, and  $\mathbf{k}^{\perp} = (-k_y, k_x)$ . A set of three wavenumbers simultaneously fulfilling the frequency and wavenumber delta functions is called resonant. The three resonance conditions in Eq. (11) restrict the integration domain onto a 2D subset of  $\mathbb{R}^6$  called the resonant manifold, with six independent branches—two for each resonance condition. The six branches have analytical solutions only in the non-rotating approximation ( $f = 0$ )<sup>35</sup>.

Here, we depart from such an approximation and treat the fully rotating problem. For the numerical integration of the collision integral Eq. (11), we use the same discretization of the  $k$ - $m$  space as in ref. 87. The change of variables to the  $m$ - $\omega$  space is obtained by using the dispersion relation Eq. (7). The search for the solutions of the six branches of the resonant manifold (see Fig. 2) with  $f \neq 0$  is performed iteratively starting from the exact solutions of the  $f = 0$  case<sup>87</sup>, using the *fzero Matlab* routine. This implies a significant increase in the computational cost compared to the non-rotating approximation.

A representation of the six-branch resonant manifold for a test wave with coordinates  $(m, \omega)$  is shown in Fig. 8, as the test wave is moved around the  $m$ - $\omega$  space. For  $\omega \gg f$ , approaching the non-rotating limit, the resonant manifold tends to the analytical non-rotating solutions<sup>35</sup>. As  $\omega \rightarrow f$ , on the contrary, the deformation of the resonant manifold becomes



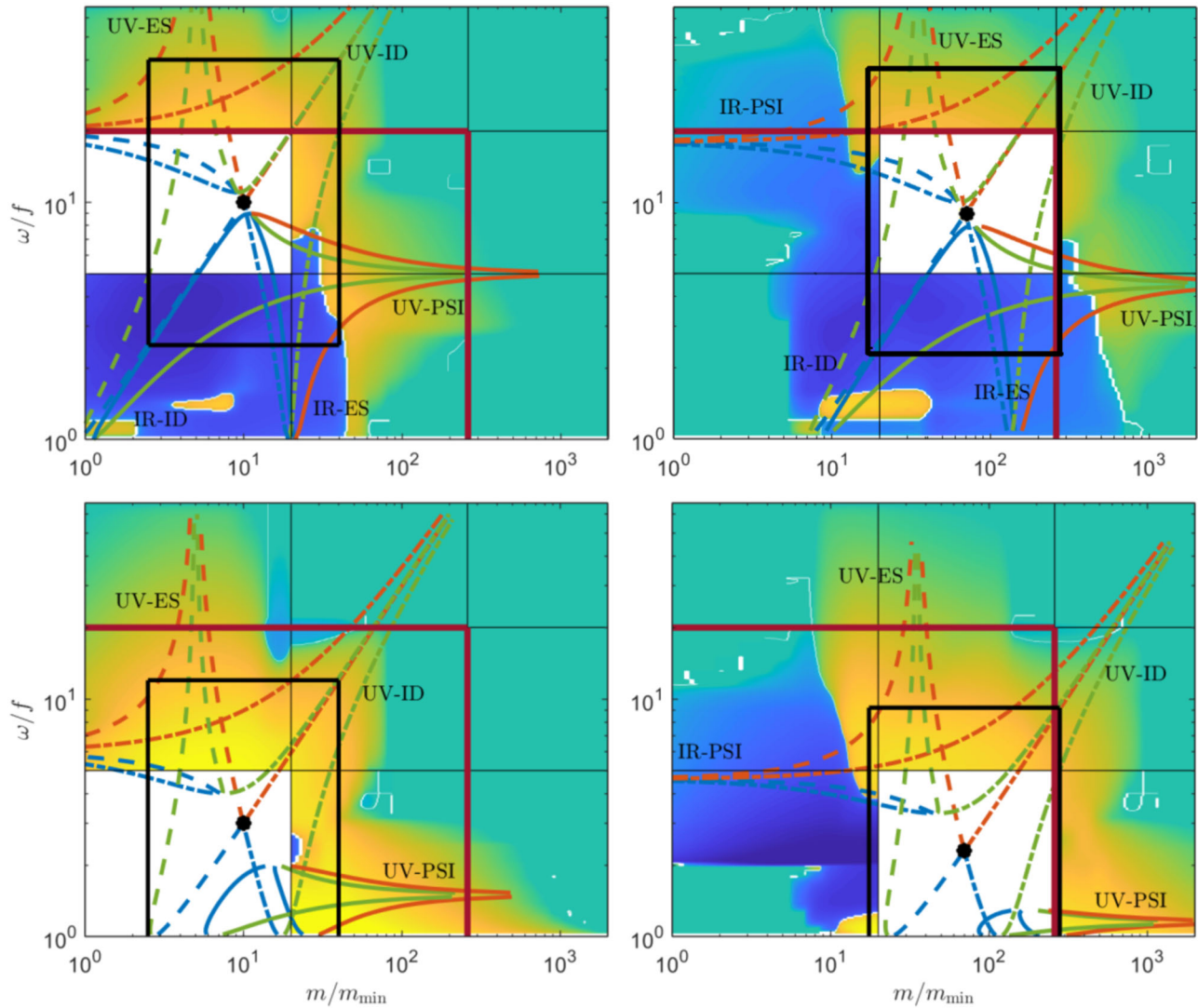


**Fig. 8 | Evaluation of energy transfers represented in spectral space.** Contribution  $I[e, e](m, \omega|B)$ , representing the energy exchange between a point  $(m, \omega)$  and set  $B$ , the white region in each of the four panels. A yellow tonality at a point  $(m, \omega)$  indicates energy directed from  $B$  to  $(m, \omega)$ , and a blue tonality the reverse. Green points have no direct energy exchange with  $B$ . The curved lines are the resonant manifold for a representative point (black dot) in set  $B$ . The matching between the resonant manifold’s lobes and the observed energy transfer patterns

allows us to discern the direction of the energy transfers associated with the different processes of Induced Diffusion (ID), Parametric Subharmonic Instability (PSI), and Elastic Scattering (ES). The ultraviolet (UV) and infrared (IR) labels indicate interaction of the test wave with waves of smaller and larger scale, respectively. The black box surrounding the test wave delimits a scale separation by a factor of 4 from the test wave, delimiting the scale-separated interactions from the spectrally-local interactions (see Fig. 2E).

apparent, and only three branches are present for  $\omega < 2f$ . A direct numerical integration over the two remaining degrees of freedom spanning the resonant manifold finally returns a numerical value for Eq. (11).

**Wave-wave interaction transfers.** Given two non-overlapping subregions of the spectral space, sets  $A$  and  $B$ , the instantaneous energy transfer from  $A$  (input control set) to  $B$  (output control set) is given by

$$P_{A \rightarrow B} = -\frac{N^2}{g} \int_A I[e, e](m, \omega|B) dm d\omega, \tag{14}$$

$$I[e, e](m_0, \omega_0|B) = J(m_0, \omega_0) \int \left[ \left( \frac{\chi_B(\mathbf{p}_1)\omega_1 + \chi_B(\mathbf{p}_2)\omega_2}{\omega_1 + \omega_2} \right) R_{10}^0 \right. \\ \left. - \chi_B(\mathbf{p}_1)R_{02}^1 - \chi_B(\mathbf{p}_2)R_{10}^2 \right] d\mathbf{p}_{12}$$

where  $I[e, e](m, \omega|B)$  captures the resonant transfers of mode  $(m, \omega) \in A$  subject to the constraint that the transfer must be between point

$(m, \omega)$  and set  $B$ <sup>59</sup>. The indicator function of set  $B$  is defined so that  $\chi_B(\mathbf{p}) = 1$  if  $\mathbf{p} \in B$  and  $\chi_B(\mathbf{p}) = 0$  otherwise. The factor  $N^2/g$  takes into account the conversion between volumes from isopycnal coordinates to Eulerian coordinates so that the energy transfers are expressed in  $W/kg$ .

In order to go from Eqs. (10) to (14), the following two steps are necessary: (i) A logical weighting that accepts only those contributions whose output wavenumbers are in the output set  $B$ , discarding the rest of the contributions; (ii) An outer supplementary 2D integration over the input set  $A$ . The method is rigorously derived in ref. 59. Here, the main innovation is the use of a  $3 \times 3$  multiscale partition of the Fourier space tailored to the oceanic internal-wave problem. A complete knowledge of the inter-scale transfers requires a permutation of all of the nine subregions of the partition in the roles of  $A$  and  $B$ , resulting into a  $9 \times 9$  energy transfer matrix—although not all elements are relevant to the analysis: e.g., we are not interested in quantifying transfers between different dissipative subregions. The matrix is anti-symmetric, satisfying some fundamental properties for a directed



transfer: (i)  $P_{A \rightarrow A} = 0$ , (ii)  $P_{A \rightarrow B} = -P_{B \rightarrow A}$ , and (iii)  $P_{A \cup B \rightarrow C} = P_{A \rightarrow C} + P_{B \rightarrow C}$  (for  $A \cup B = \emptyset$ ).

We end this section with a remark on numerical details. We use the antisymmetry of  $P_{A \rightarrow B}$  as a criterion to establish a satisfactory numerical resolution level of the spectral space, in the numerical integration. Our convergence requirement is that  $(P_{A \rightarrow B} + P_{B \rightarrow A})/P_{A \rightarrow B}$  (our measure of numerical uncertainty, as the quantity tends to zero as the resolution increases) be smaller than 5% for all elements of the transfer matrix. Using parallel computing on a 12-core station, the computation of the  $9 \times 9$  transfer matrix for a given point in parameter space  $(s_{NI}, s_{\omega}, s_m)$  takes about 6 hours. We use a numerical grid of  $5 \times 5 \times 5$  points to discretize the parameter space, for a total computing time of the order of a month. Once this computation has been performed once and stored in memory, we then use 3D interpolation to establish the flux matrix associated with any given point  $(s_{NI}, s_{\omega}, s_m)$  that is not on the numerical grid, with almost negligible extra computing time. The processing of the hundreds of thousands of spectra in the combined global data set, including both spectral slope fitting and energy transfer predictions, is performed in a few hours of computing time. All computations and plotting in the present manuscript are performed in *Matlab*.

**First-principle mixing parameterization.** The turbulent energy production rate,  $\mathcal{P}$ , is given by the sum of the energy transfers across the boundary delimiting the dissipative regions<sup>34,88</sup>. The resulting first-principles formula for  $\mathcal{P}$  reads:

$$\mathcal{P} = \mathcal{P}_0^{\text{th}}(s_{NI}, s_{\omega}, s_m) \frac{f}{f_0} \left( \frac{Em_*^{s_m-1}}{E_0 m_*^{s_m-1}} \right)^2, \quad (15)$$

where  $\mathcal{P}_0^{\text{th}}(s_{NI}, s_{\omega}, s_m)$  is a function in the 3D space of the spectral slopes.

Let us summarize the main steps leading from the primitive equations of the ocean to the formula Eq. (15) for  $\mathcal{P}$ .

- Derivation of Eq. (10) under the assumptions listed in section “Hamiltonian formalism of internal wave-wave interactions”;
- Calculation of the inter-scale energy transfers between the different subregions of the Fourier space (section “Wave-wave interaction transfers”), via Eq. (14), including the total energy transfer into the dissipative subregions, leading directly to formula Eq. (15).

The function  $\mathcal{P}_0^{\text{th}}(s_{NI}, s_{\omega}, s_m)$  is computed numerically and is represented in Fig. 7 as a colormap at five given values of  $s_m$ .  $\mathcal{P}_0^{\text{th}}$  is independent of  $m$ , because of the following approximation. As shown in Fig. 2 the direct contribution to  $\mathcal{P}$  from small wavenumbers close to  $m_*$  is nearly negligible. By the analytical properties of the GM76 spectrum<sup>41</sup>, for fixed slope  $s_m$  and total energy  $E$ , the vertical wavenumber spectrum is given by

$$e(m) = \frac{c(s_m)E(m_*)^{-1}}{1 + \left(\frac{m}{m_*}\right)^{s_m}}, \quad \text{with} \quad c(s_m) = \frac{s_m}{\Gamma\left(\frac{1}{s_m}\right)\Gamma\left(\frac{s_m-1}{s_m}\right)}, \quad (16)$$

where  $\Gamma(\cdot)$  is the gamma function (see section 2.2 of ref. 41). At high wavenumbers, we have  $e(m) \simeq Ec(s_m)(m_*)^{s_m-1}m^{-s_m}$ , for  $m \gg m_*$ . This shows that the high-wavenumber spectral level depends directly on the value of  $m_*$ , even for  $m \gg m_*$ . Thus, in order for the spectrum with the reference parameter  $m^0$  to match the high-wavenumber spectral level of a spectrum with parameter  $m_*$ , it has to be renormalized by a factor  $(m_*/m^0)^{s_m-1}$ . This explains the correction to the energy level in Eq. (15).

Here, we briefly derive a relationship between the normalized shear spectral level of Eq. (15)<sup>13</sup> and our five spectral parameters. Using Eq. (16) and the definition of shear spectral density  $S_z(m) = 2m^2 e_k(m)$ , where  $e_k(m) = e(m)R_{\omega}/(1 + R_{\omega})$ , we obtain the high wavenumber

approximation

$$S_z(m) \simeq 2 \frac{R_{\omega}}{1 + R_{\omega}} c(s_m) E m_*^{s_m-1} m^{3-s_m}. \quad (17)$$

Following<sup>13</sup>, only in this paragraph we use  $m_c$  as the high wavenumber cutoff defined via

$$\int_0^{m_c} S_z(m) dm = \frac{2\pi}{10} N_0^2. \quad (18)$$

After some algebra, using the definition of the normalized shear spectral level as  $\mathcal{E} = 0.1 \text{cpm}/m_c$ , where  $\text{cpm} = 2\pi/m$ , we arrive at

$$\mathcal{E} = \left( \frac{2\pi}{10} N_0^2 \frac{1}{2c(s_m)} \frac{1 + R_{\omega}}{R_{\omega}} \frac{3 - s_m}{E m_*^{s_m-1}} \right)^{\frac{1}{s_m-3}}. \quad (19)$$

When  $s_m = 2$ ,  $\mathcal{E} \propto E m_*$ . As a proof of consistency, if we consider the case of the standard GM76 reference parameters (which give  $c(s_m) = 2/\pi$  and  $R_{\omega} = 3$ ) we correctly obtain  $\mathcal{E} = 1$ .

In steady conditions, the turbulent energy production rate feeds the vertical buoyancy fluxes,  $\mathcal{B}$ , and the dissipation into disordered molecular motion,  $\epsilon$ :  $\mathcal{P} = \mathcal{B} + \epsilon$ . The vertical mixing diffusivity  $K$  is defined as a function of the buoyancy fluxes via  $K = \mathcal{B}/N^2$ . We use the classical Osborn parameterization<sup>89,90</sup>, establishing the proportion to be  $\mathcal{B} = R_f \mathcal{P}$ , where  $R_f \simeq 0.17$  is the flux Richardson number<sup>2</sup>. Thus, diapycnal diffusivity and turbulent dissipation rate are estimated, respectively by

$$K = \frac{R_f \mathcal{P}}{N^2}, \quad \epsilon = (1 - R_f) \mathcal{P}. \quad (20)$$

The five-parameter spectral simplification is a powerful conceptualization that turns out crucial for the realizability of our analysis in terms of numerical cost. However, in principles, any particular observed 2D spectrum can be processed individually without reduction to the five-parameter approximation. In conclusion, we can state that the calculation of  $\mathcal{P}$  from a given input spectrum is from first principles. Yet, the input from observational spectra is phenomenological due to the fitting procedure to formula Eq. (4). Indeed, also the use of Eq. (20) to pass from  $\mathcal{P}$  to the observables  $K$  and  $\epsilon$  is empirical. The problem of mixing efficiency, i.e., the ratio of  $K$  and  $\epsilon$  in stratified turbulence, is somewhat decoupled from the theoretical investigations of the present manuscript. On its own, it defines an entire area of intense research activity<sup>91–96</sup>.

**Interaction processes: classification and quantification.** An in-depth analysis of the contributions to the energy transfers allows us to identify the transfers due to each of the resonant branches with a known physical process. The numerical procedure underlying this analysis is depicted in Fig. 8 for the different spectral subregions and the different interaction classes. The resonant manifold associated with a given test wave  $(m, \omega)$  (shown in Figs. 2E and 8) has six lobes corresponding to the six resonant branches. Asymptotically, i.e., far away from the test wave, these lobes identify the three well-known scale-separated regimes of internal wave-wave interactions: ID, PSI, and ES<sup>12,60,88</sup>. Each of the three processes corresponds to two lobes: one relating the test wave to larger scales (termed ultraviolet, or UV), and the other relating the test wave to smaller scales (termed infrared, or IR). We remark that our use of the terms ID, PSI, and ES refers to the whole resonant lobes, that technically correspond to the original definition of the three classes of ref. 60 only in the asymptotic scale-separated regimes.

In Fig. 8, we represent the contribution  $\llbracket e, e \rrbracket(m, \omega|B)$  (cf. Eq. (14)) for a reference spectrum<sup>39</sup>, choosing the four non-dissipative sub-regions as set  $B$ , respectively in the four panels. The yellow color indicates wavenumbers that are gaining energy from set  $B$  (white box), while the blue color indicates wavenumbers that are transferring energy into set  $B$ . Clearly, three lobes toward smaller scales and three lobes toward larger scales (when applicable) appear in each of the panels. We superpose the curves of the resonant manifold for a representative test wave in each box to illustrate that the directions of the observed energy transfer correspond to the three main physical mechanisms of ID, PSI, and ES. Moreover, the energy transfer direction is predominantly from the IR regions (blue) to the UV regions (yellow), i.e., from the large scales to the small scales. In summary, in Fig. 8 each of the three processes is associated with a characteristic direction of energy propagation: the “energy cascade” is direct in both wavenumber and frequency for the ID branch, direct in wavenumber and slightly inverse in frequency for the PSI branch, slightly inverse in wavenumber and direct in frequency for the ES branch.

### Data availability

The analyses of the Argo data used in this manuscript are publicly available at <https://doi.org/10.5281/zenodo.6966416> and <https://doi.org/10.17882/95327>. Details on the availability of the current meter data are found in ref. 33—please contact [aleboyer@ucsd.edu](mailto:aleboyer@ucsd.edu) for further information. Details on the High-Resolution Profiler data are found in refs. 19,41.

### Code availability

The codes developed for the data analysis and theoretical computations in this manuscript are available at <https://doi.org/10.5281/zenodo.12529645><sup>97</sup>.

### References

- Ferrari, R. & Wunsch, C. Ocean circulation kinetic energy: reservoirs, sources and sinks. *Ann. Rev. Fluid Mech.* **41**, 253–282 (2008).
- Naveira Garabato, A. C. & Meredith, M. Ocean mixing: oceanography at a watershed. In *Ocean Mixing: Drivers, Mechanisms and Impacts*, Ch. 1, 1–4 (Elsevier, Amsterdam, 2022).
- Garrett, C. & Munk, W. Internal waves in the ocean. *Annu. Rev. Fluid Mech.* **11**, 339–369 (1979).
- Melet, A. V., Hallberg, R. & Marshall, D. P. The role of ocean mixing in the climate system. In *Ocean Mixing: Drivers, Mechanisms and Impacts* (eds Naveira Garabato, A. C. & Meredith, M.) Ch. 2, 5–34 (Elsevier, Amsterdam, 2022).
- de Lavergne, C., Groeskamp, S., Zika, J. & Johnson, H. L. The role of mixing in the large-scale ocean circulation. In *Ocean Mixing: Drivers, Mechanisms and Impacts*, Ch. 3, 35–63 (Elsevier, 2022).
- Cimoli, L. et al. Significance of diapycnal mixing within the Atlantic meridional overturning circulation. *AGU Adv.* **4**, 2022–000800 (2023).
- Hallberg, R., Adcroft, A., Dunne, J. P., Krasting, J. P. & Stouffer, R. J. Sensitivity of twenty-first-century global-mean steric sea level rise to ocean model formulation. *J. Clim.* **26**, 2947–2956 (2013).
- Bindoff, N.L. et al. *Changing ocean, marine ecosystems, and dependent communities*. IPCC special report on the ocean and cryosphere in a changing climate, 477–587 (IPCC, 2019)
- Song, H., Marshall, J., Campin, J.-M. & McGillicuddy Jr, D. J. Impact of near-inertial waves on vertical mixing and air-sea CO<sub>2</sub> fluxes in the southern ocean. *J. Geophys. Res.* **124**, 4605–4617 (2019).
- Whalen, C. B. et al. Internal wave-driven mixing: governing processes and consequences for climate. *Nat. Rev. Earth Environ.* **1**, 606–621 (2020).
- Olbers, D. J. Nonlinear energy transfer and the energy balance of the internal wave field in the deep ocean. *J. Fluid Mech.* **74**, 375–399 (1976).
- Müller, P., Holloway, G., Henyey, F. & Pomphrey, N. Nonlinear interactions among internal gravity waves. *Rev. Geophys.* **24**, 493–536 (1986).
- Polzin, K. L., Garabato, A. C. N., Huussen, T. N., Sloyan, B. M. & Waterman, S. Finescale parameterizations of turbulent dissipation. *J. Geophys. Res.* **119**, 1383–1419 (2014).
- MacKinnon, J. A. et al. Climate process team on internal wave-driven ocean mixing. *Bull. Am. Meteorol. Soc.* **98**, 2429–2454 (2017).
- Henyey, F. S., Wright, J. & Flatté, S. M. Energy and action flow through the internal wave field: an eikonal approach. *J. Geophys. Res.* **91**, 8487–8495 (1986).
- Gregg, M. Scaling turbulent dissipation in the thermocline. *J. Geophys. Res.* **94**, 9686–9698 (1989).
- Henyey, F.S. Scaling of internal wave model predictions for. in *Dynamics of Oceanic Internal Gravity Waves*. 233–236 (‘Aha Hulikō‘a Hawaiian Winter Workshop, 1991).
- Wijesekera, H. et al. The application of internal-wave dissipation models to a region of strong mixing. *J. Phys. Oceanogr.* **23**, 269–286 (1993).
- Polzin, K. L., Toole, J. M. & Schmitt, R. W. Finescale parameterizations of turbulent dissipation. *J. Phys. Oceanogr.* **25**, 306–328 (1995).
- Ijichi, T. & Hibiyu, T. Frequency-based correction of finescale parameterization of turbulent dissipation in the deep ocean. *J. Atmos. Ocean. Technol.* **32**, 1526–1535 (2015).
- Waterman, S., Polzin, K. L., Naveira Garabato, A. C., Sheen, K. L. & Forryan, A. Suppression of internal wave breaking in the antarctic circumpolar current near topography. *J. Phys. Oceanogr.* **44**, 1466–1492 (2014).
- Klymak, J. M., Pinkel, R. & Rainville, L. Direct breaking of the internal tide near topography: Kaena Ridge, Hawaii. *J. Phys. Oceanogr.* **38**, 380–399 (2008).
- Cusack, J. M. et al. Observed eddy–internal wave interactions in the southern ocean. *J. Phys. Oceanogr.* **50**, 3043–3062 (2020).
- Garabato, A. C. N. et al. Kinetic energy transfers between mesoscale and submesoscale motions in the open ocean’s upper layers. *J. Phys. Oceanogr.* **52**, 75–97 (2022).
- Whalen, C. B., MacKinnon, J. A. & Talley, L. D. Large-scale impacts of the mesoscale environment on mixing from wind-driven internal waves. *Nat. Geosci.* **11**, 842–847 (2018).
- Danioux, E., Vanneste, J. & Bühler, O. On the concentration of near-inertial waves in anticyclones. *J. Fluid Mech.* **773**, 2 (2015).
- Chouksey, M., Eden, C. & Olbers, D. Gravity wave generation in balanced sheared flow revisited. *J. Phys. Oceanogr.* **52**, 1351–1362 (2022).
- Whalen, C., Talley, L. & MacKinnon, J. Spatial and temporal variability of global ocean mixing inferred from Argo profiles. *Geophys. Res. Lett.* **39**, <https://doi.org/10.1029/2012GL053196> (2012).
- Waterhouse, A. F. et al. Global patterns of diapycnal mixing from measurements of the turbulent dissipation rate. *J. Phys. Oceanogr.* **44**, 1854–1872 (2014).
- Pollmann, F., Eden, C. & Olbers, D. Global finestructure estimates of internal wave energy levels and wave-induced mixing from Argo float profiles. SEANOE. <https://doi.org/10.17882/95327> (2023).
- Kunze, E. Internal-wave-driven mixing: global geography and budgets. *J. Phys. Oceanogr.* **47**, 1325–1345 (2017).
- Pollmann, F. Global characterization of the ocean’s internal wave spectrum. *J. Phys. Oceanogr.* **50**, 1871–1891 (2020).
- Le Boyer, A. & Alford, M. H. Variability and sources of the internal wave continuum examined from global moored velocity records. *J. Phys. Oceanogr.* **51**, 2807–2823 (2021).

34. Eden, C., Pollmann, F. & Olbers, D. Numerical evaluation of energy transfers in internal gravity wave spectra of the ocean. *J. Phys. Oceanogr.* **49**, 737–749 (2019).
35. Dematteis, G., Polzin, K. & Lvov, Y. V. On the origins of the oceanic ultraviolet catastrophe. *J. Phys. Oceanogr.* **52**, 597–616 (2022).
36. Olbers, D., Eden, C., Becker, E., Pollmann, F., Jungclaus, J. The IDEMIX model: parameterization of internal gravity waves for circulation models of ocean and atmosphere. In *Energy Transfers in Atmosphere and Ocean*, 87–125 (2019).
37. Melet, A., Hallberg, R., Legg, S. & Polzin, K. Sensitivity of the ocean state to the vertical distribution of internal-tide-driven mixing. *J. Phys. Oceanogr.* **43**, 602–615 (2013).
38. Zhang, H. J., Whalen, C. B., Kumar, N. & Purkey, S. G. Decreased stratification in the abyssal southwest Pacific basin and implications for the energy budget. *Geophys. Res. Lett.* **48**, 2021–094322 (2021).
39. Cairns, J. L. & Williams, G. O. Internal wave observations from a midwater float. *J. Geophys. Res.* **81**, 1943–1950 (1976).
40. Alford, M. H. & Whitmont, M. Seasonal and spatial variability of near-inertial kinetic energy from historical moored velocity records. *J. Phys. Oceanogr.* **37**, 2022–2037 (2007).
41. Polzin, K.L. & Lvov, Y. V. Toward regional characterizations of the oceanic internal wavefield. *Rev. Geophys.* **49**, RG4003 (2011).
42. Holloway, G. Oceanic internal waves are not weak waves. *J. Phys. Oceanogr.* **10**, 906–914 (1980).
43. Lvov, Y. V. & Tabak, E. A Hamiltonian formulation for long internal waves. *Phys. D.* **195**, 106 (2004).
44. Zakharov, V.E., L'vov, V. S. & Falkovich, G. *Kolmogorov Spectra of Turbulence* (Springer, Berlin, 1992).
45. Nazarenko, S. *Wave Turbulence* (Springer, Heidelberg, 2011).
46. Galtier, S. *Physics of Wave Turbulence* (Cambridge University Press, 2022). Google-Books-ID: TXmaEAAQBAJ
47. Sun, H. & Kunze, E. Internal wave–wave interactions. Part ii: spectral energy transfer and turbulence production. *J. Phys. Oceanogr.* **29**, 2905–2919 (1999).
48. Ijichi, T. & Hibiya, T. Eikonal calculations for energy transfer in the deep-ocean internal wave field near mixing hotspots. *J. Phys. Oceanogr.* **47**, 199–210 (2017).
49. Lvov, Y. V. & Polzin, K. L. Generalized transport characterizations for short oceanic internal waves in a sea of long waves. *J. Fluid Mech.* **987**, 43 (2024).
50. Polzin, K.L. & Lvov, Y.V. A one-dimensional model for investigating scale-separated approaches to the interaction of oceanic internal waves. *arXiv preprint arXiv:2204.00069* (2022).
51. Olbers, D., Willebrand, J., Eden, C. *Ocean Dynamics* (Springer, Berlin Heidelberg, 2012).
52. MacKinnon, J. et al. Parametric subharmonic instability of the internal tide at 29°N. *J. Phys. Oceanogr.* **43**, 17–28 (2013).
53. MacKinnon, J. & Winters, K. Subtropical catastrophe: significant loss of low-mode tidal energy at 28.9°. *Geophys. Res. Lett.* **32**, L15605 (2005).
54. Skitka, J. et al. Probing the nonlinear interactions of supertidal internal waves using a high-resolution regional ocean model. *J. Phys. Oceanogr.* **54**, 399–425 (2024).
55. Rodda, C. et al. Experimental observations of internal wave turbulence transition in a stratified fluid. *Phys. Rev. Fluids* **7**, 094802 (2022).
56. Lanchon, N., Mora, D. O., Monsalve, E. & Cortet, P.-P. Internal wave turbulence in a stratified fluid with and without eigenmodes of the experimental domain. *Phys. Rev. Fluids* **8**, 054802 (2023).
57. Wu, Y., Kunze, E., Tandon, A. & Mahadevan, A. Reabsorption of lee-wave energy in bottom-intensified currents. *J. Phys. Oceanogr.* **53**, 477–491 (2023).
58. Yang, L. et al. Oceanic eddies induce a rapid formation of an internal wave continuum. *Commun. Earth Environ.* **4**, 1–10 (2023).
59. Dematteis, G. & Lvov, Y. V. The structure of energy fluxes in wave turbulence. *J. Fluid Mech.* **954**, 30 (2023).
60. McComas, C. H. & Bretherton, F. P. Resonant interaction of oceanic internal waves. *J. Geophys. Res.* **83**, 1397–1412 (1977).
61. Wu, Y. & Pan, Y. Energy cascade in the Garrett–Munk spectrum of internal gravity waves. *J. Fluid Mech.* **975**, A11 (2023).
62. Onuki, Y. & Hibiya, T. Decay rates of internal tides estimated by an improved wave–wave interaction analysis. *J. Phys. Oceanogr.* **48**, 2689–2701 (2018).
63. Musgrave, R., Pollmann, F., Kelly, S. & Nikurashin, M. The lifecycle of topographically-generated internal waves. In *Ocean Mixing: Drivers, Mechanisms and Impacts* (eds Naveira Garabato, A. C. & Meredith, M.) Ch. 6, 117–144 (Elsevier, Amsterdam, 2022).
64. Polzin, K., Toole, J., Ledwell, J. & Schmitt, R. Spatial variability of turbulent mixing in the abyssal ocean. *Science* **276**, 93–96 (1997).
65. Kunze, E., Schmitt, R. W. & Toole, J. M. The energy balance in a warm-core ring's near-inertial critical layer. *J. Phys. Oceanogr.* **25**, 942–957 (1995).
66. Whalen, C. B., MacKinnon, J. A., Talley, L. D. & Waterhouse, A. F. Estimating the mean diapycnal mixing using a finescale strain parameterization. *J. Phys. Oceanogr.* **45**, 1174–1188 (2015).
67. Olbers, D., Pollmann, F. & Eden, C. On psi interactions in internal gravity wave fields and the decay of baroclinic tides. *J. Phys. Oceanogr.* **50**, 751–771 (2020).
68. Broutman, D. On internal wave caustics. *J. Phys. Oceanogr.* **16**, 1625–1635 (1986).
69. Broutman, D. & Young, W. On the interaction of small-scale oceanic internal waves with near-inertial waves. *J. Fluid Mech.* **166**, 341–358 (1986).
70. D'Asaro, E. A. & Lien, R.-C. The wave–turbulence transition for stratified flows. *J. Phys. Oceanogr.* **30**, 1669–1678 (2000).
71. Rodda, C. et al. From internal waves to turbulence in a stably stratified fluid. *Phys. Rev. Lett.* **131**, 264101 (2023).
72. Zachary, T. et al. Experimental investigation of tidally-forced internal wave turbulence at high Reynolds number. *arXiv preprint arXiv:2408.05593* (2024).
73. Furue, R. Energy transfer within the small-scale oceanic internal wave spectrum. *J. Phys. Oceanogr.* **33**, 267–282 (2003).
74. Pan, Y. et al. Numerical investigation of mechanisms underlying oceanic internal gravity wave power-law spectra. *J. Phys. Oceanogr.* **50**, 2713–2733 (2020).
75. Hibiya, T., Niwa, Y., Nakajima, K. & Sugimoto, N. Direct numerical simulation of the roll-off range of internal wave shear spectra in the ocean. *J. Geophys. Res.* **101**, 14123–14129 (1996).
76. Bel, G. & Tziperman, E. Is the resonant wave interaction approximation consistent with the dynamics of internal wave fields? *arXiv preprint arXiv:2207.02758* (2022).
77. Barkan, R. et al. Oceanic mesoscale eddy depletion catalyzed by internal waves. *Geophys. Res. Lett.* **48**, 2021–094376 (2021).
78. Eyink, G. L. & Aluie, H. Localness of energy cascade in hydrodynamic turbulence. i. smooth coarse graining. *Physics of Fluids* **21**, 115107 (2009).
79. Wong, A. P. et al. Argo data 1999–2019: Two million temperature–salinity profiles and subsurface velocity observations from a global array of profiling floats. *Front. Mar. Sci.* **7**, 700 (2020).
80. Kunze, E., Firing, E., Hummon, J. M., Chereskin, T. K. & Thurnherr, A. M. Global abyssal mixing inferred from lowered adcp shear and CTD strain profiles. *J. Phys. Oceanogr.* **36**, 1553–1576 (2006).
81. Pollmann, F., Eden, C. & Olbers, D. Evaluating the global internal wave model IDEMIX using finestructure methods. *J. Phys. Oceanogr.* **47**, 2267–2289 (2017).
82. Pollmann, F. Global characterization of the ocean's internal gravity wave vertical wavenumber spectrum from Argo float profiles. Zenodo. <https://doi.org/10.5281/zenodo.6966416> (2022).



83. Schmit, R. W., Toole, J. M., Koehler, R. L., Mellinger, E. C. & Doherty, K. W. The development of a fine-and microstructure profiler. *J. Atmos. Ocean. Technol.* **5**, 484–500 (1988).
  84. Vallis, G.K. *Atmospheric and Oceanic Fluid Dynamics* (Cambridge University Press, Cambridge, U.K., 2017).
  85. Hasselmann, K. Feynman diagrams and interaction rules of wave-wave scattering processes. *Rev. Geophys.* **4**, 1–32 (1966).
  86. Lvov, Y. V., Tabak, E., Polzin, K. L. & Yokoyama, N. The oceanic internal wavefield: theory of scale invariant spectra. *J. Phys. Oceanogr.* **40**, 2605–2623 (2010).
  87. Dematteis, G. & Lvov, Y. V. Downscale energy fluxes in scale-invariant oceanic internal wave turbulence. *J. Fluid Mech.* **915**, 129 (2021).
  88. McComas, C. H. & Müller, P. The dynamic balance of internal waves. *J. Phys. Oceanogr.* **11**, 970–986 (1981).
  89. Osborn, T. Estimates of the local rate of vertical diffusion from dissipation measurements. *J. Phys. Oceanogr.* **10**, 83–89 (1980).
  90. Thorpe, S. A. Recent developments in the study of ocean turbulence. *Annu. Rev. Earth Planet. Sci.* **32**, 91–109 (2004).
  91. Peltier, W. & Caulfield, C. Mixing efficiency in stratified shear flows. *Annu. Rev. Fluid Mech.* **35**, 135–167 (2003).
  92. Bluteau, C., Jones, N. & Ivey, G. Turbulent mixing efficiency at an energetic ocean site. *J. Geophys. Res.: Oceans* **118**, 4662–4672 (2013).
  93. Maffioli, A., Brethouwer, G. & Lindborg, E. Mixing efficiency in stratified turbulence. *J. Fluid Mech.* **794**, 3 (2016).
  94. Ijichi, T. & Hibiya, T. Observed variations in turbulent mixing efficiency in the deep ocean. *J. Phys. Oceanogr.* **48**, 1815–1830 (2018).
  95. Gregg, M. C., D’Asaro, E. A., Riley, J. J. & Kunze, E. Mixing efficiency in the ocean. *Annu. Rev. Mar. Sci.* **10**, 443–473 (2018).
  96. Ijichi, T., St. Laurent, L., Polzin, K. L. & Toole, J. M. How variable is mixing efficiency in the abyss? *Geophys. Res. Lett.* **47**, 2019–086813 (2020).
  97. Dematteis, G. Codes for ‘Interacting internal waves explain global patterns of interior ocean mixing’ (v1.0). Zenodo. <https://doi.org/10.5281/zenodo.12529645> (2024).
- Forschungsgemeinschaft (DFG, German Research Foundation)—Projektnummer 274762653. C.W. was funded by OCE-2048660 and ONR-N00014-18-1-2598.

### Author contributions

G.D. performed the theoretical/numerical calculations with support from Y.L. A.L.B., F.P., and G.D. developed the data analysis to build the global combined dataset of 2D internal wave spectra. G.D. and K.P. performed the HRP data analysis. G.D., F.P., and A.L.B. wrote the first draft of the manuscript. G.D., A.L.B., F.P., K.P., M.A., C.W., and Y.L. contributed to designing the research, drafting sections, and revising the manuscript.

### Competing interests

The authors declare no competing interests.

### Additional information

**Supplementary information** The online version contains supplementary material available at <https://doi.org/10.1038/s41467-024-51503-6>.

**Correspondence** and requests for materials should be addressed to Giovanni Dematteis.

**Peer review information** *Nature Communications* thanks the anonymous reviewers for their contribution to the peer review of this work. A peer review file is available.

**Reprints and permissions information** is available at <http://www.nature.com/reprints>

**Publisher’s note** Springer Nature remains neutral with regard to jurisdictional claims in published maps and institutional affiliations.

**Open Access** This article is licensed under a Creative Commons Attribution-NonCommercial-NoDerivatives 4.0 International License, which permits any non-commercial use, sharing, distribution and reproduction in any medium or format, as long as you give appropriate credit to the original author(s) and the source, provide a link to the Creative Commons licence, and indicate if you modified the licensed material. You do not have permission under this licence to share adapted material derived from this article or parts of it. The images or other third party material in this article are included in the article’s Creative Commons licence, unless indicated otherwise in a credit line to the material. If material is not included in the article’s Creative Commons licence and your intended use is not permitted by statutory regulation or exceeds the permitted use, you will need to obtain permission directly from the copyright holder. To view a copy of this licence, visit <http://creativecommons.org/licenses/by-nc-nd/4.0/>.

© The Author(s) 2024

### Acknowledgements

Discussions with D. Olbers, S. Purkey, A. Thurnherr, Y. C. Wu, Y. Pan, and J. Skitka are gratefully acknowledged. We acknowledge the International Argo Program and the national programs that contribute to it. (<https://argo.ucsd.edu>, <https://www.ocean-ops.org>). We would like to acknowledge the scientists and technicians preparing, deploying, and recovering the moorings, whose data are collected in the GMACMD database. We would also like to acknowledge the captains and crews of the many research vessels supporting all of these missions. G.D. and Y.V.L. gratefully acknowledge funding from NSF DMS award 2009418. G.D. and K.P. gratefully acknowledge funding from grant OCE-83243900. G.D. and Y.V.L. acknowledge funding from the Simons Foundation through the Simons Collaboration on Wave Turbulence. F.P. acknowledges the Collaborative Research Centre TRR 181 “Energy Transfers in Atmosphere and Ocean” funded by the Deutsche